Large-area high spatial resolution albedo retrievals from remote sensing for use in assessing the impact of wildfire soot deposition on high mountain snow and ice melt

André Bertoncini [*], Caroline Aubry-Wake, John W. Pomeroy

Centre for Hydrology, University of Saskatchewan, 116A-1151 Sidney Street, Canmore, AB T1W 3G1, Canada

ARTICLE INFO

ABSTRACT

Soot deposition from wildfires decreases snow and ice albedo and increases the absorption of shortwave radiation, which advances and accelerates melt. Soot deposition also induces algal growth, which further decreases snow and ice albedo. In recent years, increasingly severe and widespread wildfire activity has occurred in western Canada in association with climate change. In the summers of 2017 and 2018, westerly winds transported smoke from extensive record-breaking wildfires in British Columbia eastward to the Canadian Rockies, where substantial amounts of soot were deposited on high mountain glaciers, snowfields, and icefields. Several studies have addressed the problem of soot deposition on snow and ice, but the spatiotemporal resolution applied has not been compatible with studying mountain icefields that are extensive but contain substantial internal variability and have dynamical albedos. This study evaluates spatial patterns in the albedo decrease and net shortwave radiation (K*) increase caused by soot from intense wildfires in Western Canada deposited on the Columbia Icefield (151 km^2), Canadian Rockies, during 2017 and 2018. Twelve Sentinel-2 images were used to generate high spatial resolution albedo retrievals during four summers (2017 to 2020) using a MODIS bidirectional reflectance distribution function (BRDF) model, which was employed to model the snow and ice reflectance anisotropy. Remote sensing estimates were evaluated using site-measured albedo on the icefield's Athabasca Glacier tongue, resulting in a R^2, mean bias, and root mean square error (RMSE) of 0.68, 0.019, and 0.026, respectively. The biggest inter-annual spatially averaged soot-induced albedo declines were of 0.148 and 0.050 (2018 to 2020) for southeast-facing glaciers and the snow plateau, respectively. The highest inter-annual spatially-averaged soot-induced shortwave radiative forcing was 203 W/m^2 for southeast-facing glaciers (2018 to 2020) and 106 W/m^2 for the snow plateau (2017 to 2020). These findings indicate that snow albedo responded rapidly to and recovered rapidly from soot deposition. However, ice albedo remained low the year after fire, and this was likely related to a bio-albedo feedback involving microorganisms. Snow and ice K* were highest during low albedo years, especially for south-facing glaciers. These large-scale effects accelerated melt of the Columbia Icefield. The findings highlight the importance of using large-area high spatial resolution albedo estimates to analyze the effect of wildfire soot deposition on snow and ice albedo and K* on icefields, which is not possible using other approaches.

1. Introduction

High mountain regions form the headwaters of major river basins around the world, and they provide critical water supplies for nearly 40% of the global population (Viviroli et al., 2020). The Canadian Rockies are situated on a triple point continental divide that forms the headwaters of the Saskatchewan-Nelson, Fraser and Columbia, and Peace-Athabasca-Mackenzie rivers, which flow to the Atlantic, Pacific, and Arctic oceans, respectively, and provide vital water sources for vast regions of North America. This mountain range is crowned with permanent snow and glaciers, and amongst other processes, the absorption of solar radiation in spring and summer governs the annual volume of available meltwater that forms streamflow and the subsequent downstream water supply.

Climate change has decreased glacier volume and area (Tennant and Menounos, 2013) and increased the amount of water released by these

---

major icefields steadily (Bolch et al., 2010; Hopkinson and Young, 1998). In addition, climate change is also affecting environmental conditions that lead to wildfires (Jolly et al., 2015). An increase in the frequency and intensity of wildfires has been noted in western Canada (Hanes et al., 2019) and globally (Seidl et al., 2017). Besides localized impacts, the spread of smoke has a cascading effect that has trans-continental impacts (Baars et al., 2019; Chen et al., 2019), but larger smoke particles are deposited as soot in a more regional context (Kim et al., 2005). Intense wildfire seasons occurred in British Columbia (BC) in the summers of 2017 and 2018 (Kirchmeier-Young et al., 2019). The prevailing westerly wind flow in the region in association with the wildfires in the central BC forests rapidly spread smoke across Canada, and soot was deposited on the nearby Canadian Rockies. An increase in soot deposition from wildfires can decrease snow and ice albedo and increase the shortwave radiation absorption and melt of these surfaces (Ebrahimi and Marshall, 2016). In this study, the term "snow and ice" is used interchangeably to describe snow (albedo typical range: 0.40 to 0.85), firn (0.30 to 0.55), and ice (0.20 to 0.65) (Cuffey and Paterson, 2010).

Several studies have analyzed the hydrological implications of increases in the deposition of dust and soot over snow and ice on small scales (e.g., Doherty et al., 2010; Kaspari et al., 2015; de Magalhães et al., 2019; McKenzie Skiles et al., 2018; Nagorski et al., 2019), using either intensive fieldwork or automatic weather station (AWS) observations. A recent small-scale study showed evidence of substantial albedo spatial variations due to dust deposition, which, together with complex interactions between slope and aspect, have an impact on the scalability of melt rate calculations (Schirmer and Pomeroy, 2020), and this is also expected to apply to soot deposition. Large-scale studies have used coarse-resolution modelling (1° to 2.8°) (e.g., Flanner et al., 2009, 2007; Yasunari et al., 2013) or remote sensing spatiotemporal analysis from the Moderate Resolution Imaging Spectroradiometer (MODIS) (~ 500 m) (e.g., Lee and Liou, 2012; Mortimer and Sharp, 2018; Painter et al., 2012; Williamson and Menounos, 2021), which cannot detect small-scale variations that may be important in a mountain environment. Small- and large-scale studies have inherent disadvantages. For example, although small-scale studies are essential for enhancing our understanding of snow and ice albedo, they lack the spatial coverage of large-scale studies. Therefore, employing high spatial resolution optical imagery (i.e., with a 20 to 30 m spatial resolution) would help in solving both scale and coverage issues and providing sufficient spatial detail to enable snow and ice energy fluxes to be described, while using a spatial coverage that can enable the consistent monitoring of large mountain icefields at one overpass.

In addition to scale and coverage effects, studies monitoring snow and ice albedo also need to consider that their reflectance varies with solar and viewing angles due to anisotropy. Snow and ice surfaces differ from most vegetation-soil systems in that their reflectance is higher when the sun is in the opposite direction of the sensor (when forward-scattering occurs), rather than being higher when the sun is behind the sensor (during which backward-scattering occurs) (Jiao et al., 2019). Anisotropy can be represented using a bidirectional reflectance distribution function (BRDF). The BRDF for vegetation-soil systems is well represented by the RossThick-LiSparseReciprocal (RTLSR) kernel model (Li et al., 2001; Roujean et al., 1992; Wanner et al., 1995), which is currently used in the MODIS albedo retrieval algorithm (MCD43A1) (Lucht et al., 2000; Schaaf et al., 2002) that is used to monitor Earth's albedo worldwide, and it has been successful for some snow and ice applications (Li et al., 2018; Mortimer and Sharp, 2018; Wang et al., 2016). However, the RTLSR model is not optimal for describing the reflectance behavior of snow and ice surfaces because it favors the representation of backward-scattering instead of forward-scattering. Jiao et al. (2019) enhanced the RTLSR model by adding a snow kernel, which improved the BRDF representation of surfaces covered by pure snow. It is also possible to retrieve the BRDF of snow (Lee and Liou, 2012) using empirical look-up-tables (LUTs) (Stamnes et al., 1988), but

this information cannot account for variations in albedo due to soot deposition.

Downscaling techniques have been employed to resolve scale issues from MODIS to Landsat/Sentinel-2 spatial resolution. Shuai et al. (2011) developed the precursor of currently applied albedo downscaling techniques. Shuai et al.'s (2011) technique relies on the translation of spectral similarity between MODIS and Landsat homogenous pixels into BRDF similarity. Although this technique was ground-breaking, it did not retrieve high spatial resolution albedo over snow-covered surfaces due to radiometric limitations of pre-Landsat 8-OLI high spatial resolution operational sensors. Wang et al. (2016) later applied this technique to snow-covered surfaces to analyze the effects of wildfire on early spring boreal forest albedo, since the improvements on Landsat 8-OLI radiometric resolution reduced saturation over snow pixels. Sentinel-2 has reduced the saturation of snow pixels even more, and therefore, Li et al. (2018) were able to use Sentinel-2 albedo retrievals over snow for the first time. All these applications have used the RTLSR model with some success, but the use of a snow and ice BRDF model downscaled to high resolutions has not yet been employed to assess the impacts of wildfires on snow and ice albedo and net shortwave radiation (K*). Several studies have addressed the estimation of land surface energy balance at Landsat spatial resolution or finer, including K*, but they are either applied to evapotranspiration (e.g., Bastiaanssen et al., 1998; Allen et al., 2007) or are heavily empirical and do not account explicitly for the effects of BRDF on K* estimation (e.g., Duguay, 1995; Painter et al., 2013; Wang et al., 2014).

The purpose of this paper is to assess the impact of soot deposition from wildfire on albedo and K* over the Columbia Icefield in the Canadian Rockies. The specific objectives of this study are to: develop a generalized method that permits high spatial resolution albedo retrievals over mountains with snow and ice cover; use the method to determine the temporal and spatial evolution of the impacts of soot on the albedo of a mountain icefield; and apply these results to determine the spatial persistence of shortwave radiative forcing of wildfire soot on mountain snow and ice surfaces, including consideration of the impact of slope and aspect. To achieve these objectives, an albedo retrieval framework that uses a BRDF reflectance model coupled with a downscaling technique is developed to retrieve snow and ice albedo at a Sentinel-2 20 m spatial resolution. High spatial resolution albedo retrievals over glacierized mountain snow and ice can contribute to the spatiotemporal monitoring of albedo changes induced by climate change, such as those caused by wildfire soot deposition.

2. Material and methods

2.1. Study area

The study area is the Columbia Icefield, which sits astride the continental divide in the Canadian Rockies (Fig. 1). This icefield is the largest in the Rocky Mountains (Heusser, 1956) and it is extremely important for providing the water resources of four major North American river basins: Saskatchewan-Nelson, Fraser, Columbia, and Peace-Athabasca-Mackenzie. It is particularly important for sustaining flows in late summer, when glacier melt contribution to streamflow is high. The icefield had an area of 205.5 km^2 in 2009, a 23% decline from 1919, with the most rapid rate of decline from 2000 to 2009 (Tennant and Menounos, 2013). Elevations range from ~1700 to 3700 m above mean sea level (a.m.s.l.), as estimated by the National Aeronautics and Space Administration's (NASA) Shuttle Radar Topography Mission (SRTM). The icefield's current mean annual temperature is −4 °C and total annual precipitation is 1277 mm (Tennant and Menounos, 2013). The lower-right corner inset map in Fig. 1 shows the area of interest (AOI) for MODIS data sampling, which was expanded to provide a higher number of snow and ice pixels for the MODIS BRDF modelling; however, all high spatial resolution albedo analyses were focused on the Columbia Icefield surface.
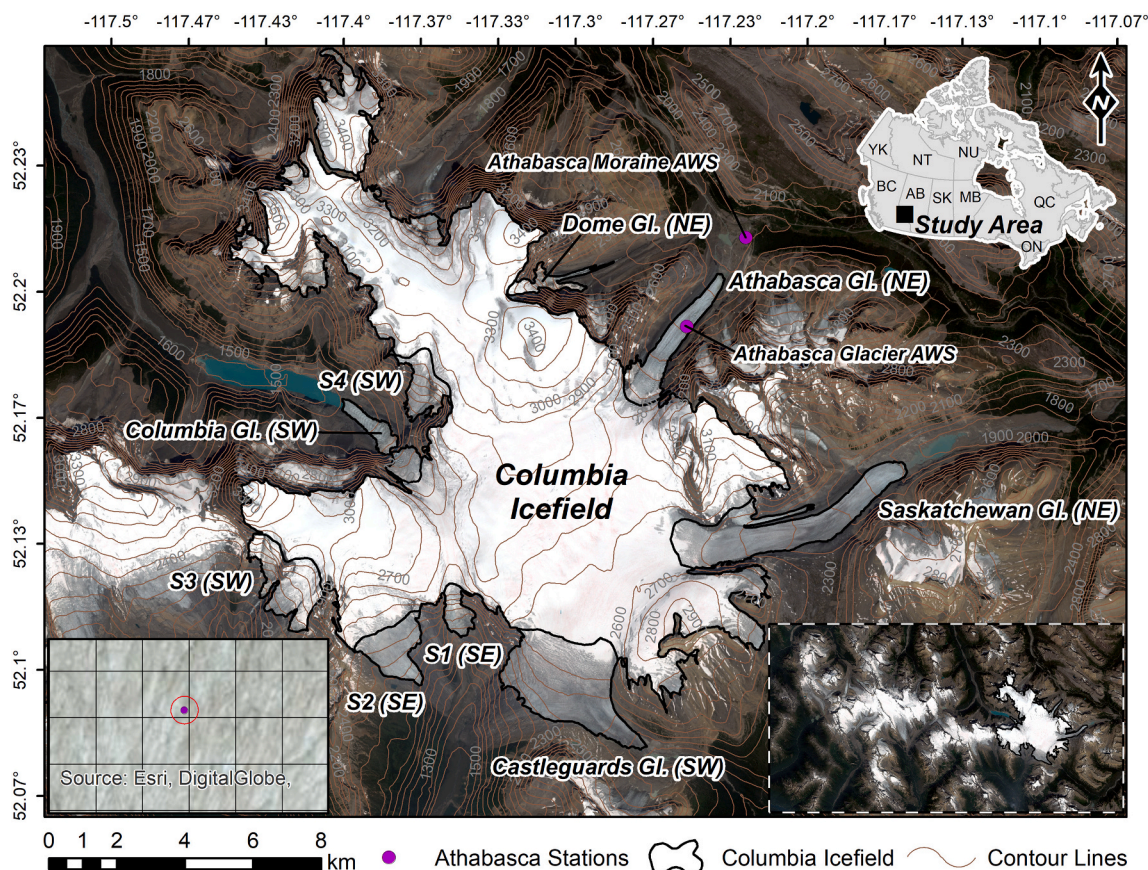
Fig. 1. Study area map showing the Columbia Icefield, its outlet glaciers, the AWS used in the study, and terrain contour lines from SRTM (Feb. 2000). The map inset in the lower-right corner shows the AOI for Sentinel-2 cloud screening and MODIS pixel sampling. The map inset in the lower-left corner shows the Athabasca Glacier AWS albedometer footprint in red and the Sentinel-2 grid in black – the high spatial resolution RGB image is from Esri satellite basemap (image date: 2020-06-25). The map also shows the glacier mean aspect and boundaries used to compute spatial averages. Small south-facing glaciers were called S1 to S4. RGB coloured Sentinel-2 image is from 2018-08-08. (For interpretation of the references to colour in this figure legend, the reader is referred to the web version of this article.)

The study was conducted between July 1 and September 15 during 2016, 2017, 2018, 2019, and 2020. During these periods, the AWSs of the Athabasca Glacier (2177 m a.m.s.l.) and Athabasca Moraine (1966 m a.m.s.l.) measured air temperature, relative humidity (Rotronic HC2-S3), precipitation (Ott Pluvio with Alter wind shield, only in the Athabasca Moraine AWS), short-and longwave radiation (Kipp and Zonen, CNR4), and albedo. The Athabasca Glacier AWS albedometer is at 1.59 m above the glacier ice, and has a 150° field of view from the upwelling shortwave radiometer, resulting in a 110 m² footprint (Fig. 1). Although the albedometer and Sentinel-2 400 m² footprints do not exactly match, both footprints cover the same lower glacier ice surface and are within an autocorrelated distance of 50 m (Arnold and Rees, 2003). A timelapse camera facing the Athabasca Glacier was also used in the analysis. These stations are operated by the University of Saskatchewan Centre for Hydrology to provide information on the glacier and proglacial surface meteorological conditions. Three Alter-shielded weighing precipitation gauges (Saskatchewan River Crossing 2, Job Creek, and Southesk) from the Alberta Agriculture and Forestry's Alberta Climate Information System (ACIS) were used to fill missing precipitation data using an inverse distance weighing interpolation method. Precipitation at Athabasca Moraine AWS was corrected for snowfall undercatch following the methods of Harder and Pomeroy (2013) for phase determination and Smith (2007) for Alter shield undercatch of snowfall. The average and accumulation values during the 2.5-month annual study periods are shown in Table 1. Note that hereafter [ ] is used as a convention to represent albedo as a unitless quantity and that numerical dates will be presented in the YYYY-MM-DD format.

Table 1

Meteorological conditions during the July 1 – September 15 study period from 2016 to 2020. The mean albedo was calculated excluding episodes of fresh snow to represent the annual albedo of glacier ice.

Variable	2016	2017	2018	2019	2020
Mean temperature [°C]	5.9	7.7	6.5	6.6	6.9
Mean relative humidity [%]	72	61	66	70	65
Total precipitation [mm]	144	91	142	131	116
Mean incoming shortwave [W/m²]	192	207	208	206	221
Mean incoming longwave [W/m²]	305	297	300	304	302
Mean albedo [ ]	0.29	0.26	0.27	0.22	0.25

2.2. General workflow for high spatial resolution albedo retrieval

Fig. 2 illustrates the general workflow used to retrieve high spatial resolution snow and ice albedo estimates. This workflow builds upon that presented in Shuai et al. (2011) and Li et al. (2018), in which the main difference is associated with testing two different BRDF models. The subsequent sections of this paper describe details of the method employed, but a brief overview is given as follows: the method first uses inverse modelling based on two different BRDF model approaches to retrieve the parameters $f_{iso}(\lambda)$, $f_{vol}(\lambda)$, and $f_{geo}(\lambda)$, for the RTLSR model; and with addition of $f_{snow}(\lambda)$, for the snow kernel model, or $f_k(\lambda)$ – the subscript k representing each kernel. These parameters are used to calculate BRDF reflectance based on Sentinel-2 near-nadir geometry information (i.e., directional illumination and directional reflectance), black-sky (i.e., directional illumination and hemispherical reflectance),
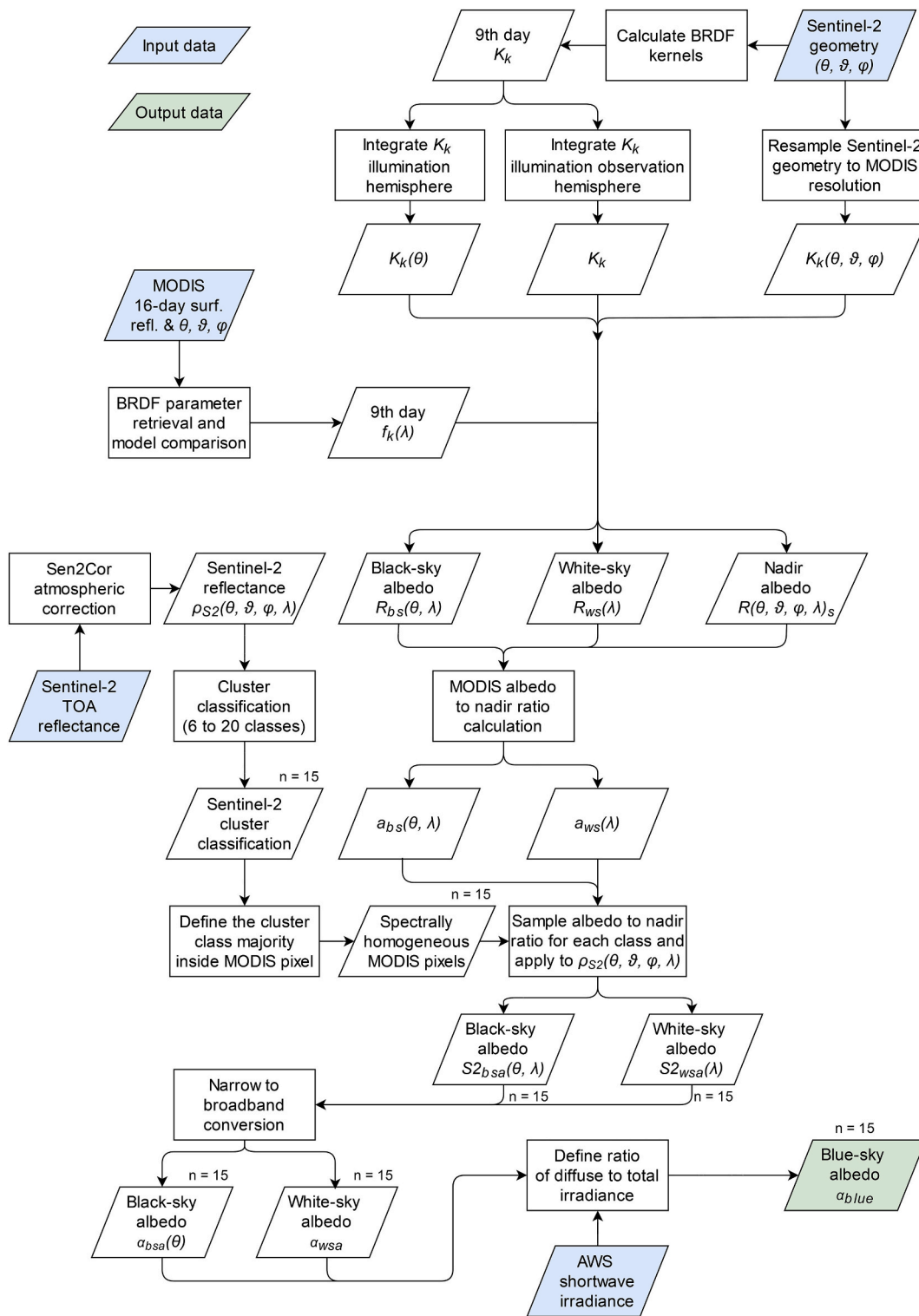
Fig. 2. Flowchart showing the general framework used in the retrieval of high spatial resolution albedo.

and white-sky (i.e., hemispherical illumination and hemispherical reflectance) spectral albedos. The model with the best BRDF estimates (RTLSR or snow kernel) is then used to calculate the ratios between black-sky/nadir and white-sky/nadir. At this point, the ratios are stored, and the processing of Sentinel-2 images begins. In this respect, Sentinel-2 top-of-atmosphere (TOA) reflectance images are first atmospherically corrected using the Sen2Cor v2.8 model (Mueller-Wilm et al., 2019), and 15 unsupervised classifications are performed, varying the number

of cluster classes from 6 to 20. This iterative process aims to find a number of cluster classes that represents reflectance seasonality for the icefield every 15 days; therefore, all the remaining high spatial resolution steps are generated 15 times. This cluster classification defines the degree of homogeneity for the selection of MODIS pixels and the sampling of previously defined black-sky and white-sky ratios. In this step, the ratio based on MODIS is sampled only for pixels that are covered by more than 60% of the same Sentinel-2 cluster class, following the

method of Shuai et al. (2011) and Li et al. (2018). This process ensures that the ratio is sampled only for relatively homogenous pixels, but the ratio is applied to all 20 m Sentinel-2 surface reflectance pixels. For example, the MODIS ratio computed for cluster class number 1 is applied to all Sentinel-2 pixels classified as cluster number 1. This downscaling technique generates two Sentinel-2 spectral albedo retrievals, black-sky and white-sky, for each number of cluster classes. A narrow-to-broad band conversion function is applied to retrieve spectrally integrated black-sky and white-sky albedos. Finally, these two retrievals are linearly interpolated based on the ratio between the surface-observed shortwave irradiance (at Athabasca Glacier AWS) and theoretically modelled shortwave irradiance, resulting in the blue-sky albedo.

2.3. BRDF modelling

Traditionally, the BRDF is modelled using the RTLSR kernel model (Li and Strahler, 1992; Roujean et al., 1992; Wanner et al., 1995), which was initially developed to model the BRDF for vegetation-soil systems $R(\theta, \vartheta, \varphi, \lambda)_v$. The original RTLSR model comprises the following three kernels,

$$R(\theta, \vartheta, \varphi, \lambda)_v = f_{iso}(\lambda) + f_{vol}(\lambda)K_{vol}(\theta, \vartheta, \varphi) + f_{geo}(\lambda)K_{geo}(\theta, \vartheta, \varphi), \quad (1)$$

where $f_{iso}(\lambda)$, $f_{vol}(\lambda)$, and $f_{geo}(\lambda)$ are the parameters of each model kernel representing isotropic, volumetric, and geometric scattering, respectively. Isotropic scattering occurs only when both sensor and illumination source are at nadir, i.e., solar zenith (θ) and sensor zenith (ϑ) = 0, and there are thus no angular effects (Shuai et al., 2011). Volumetric scattering is caused by the Lambertian reflectance of multiple small elements inside a volume that represents a vegetation canopy, and geometric scattering is caused by the reflectance of the protrusions and their shadows cast on the surface; $K_{vol}(\theta, \vartheta, \varphi)$ and $K_{geo}(\theta, \vartheta, \varphi)$ are the volumetric and geometric kernels, respectively. The model is also a function of the relative azimuth (φ), the angle between the sensor and the illumination source in the azimuth dimension, and it is wavelength dependent (λ) (Roujean et al., 1992). The formulae to calculate the volumetric and geometric kernels can be found in Li and Strahler (1992), Roujean et al. (1992), and Wanner et al. (1995).

To better represent the BRDF properties of snow and ice, the snow kernel model of Jiao et al. (2019) was also adopted, and this adds another kernel to the RTLSR equation,

$$R(\theta, \vartheta, \varphi, \lambda)_s = f_{iso}(\lambda) + f_{vol}(\lambda)K_{vol}(\theta, \vartheta, \varphi) + f_{geo}(\lambda)K_{geo}(\theta, \vartheta, \varphi) \\ + f_{snow}(\lambda)K_{snow}(\theta, \vartheta, \varphi). \quad (2)$$

In this context, the snow kernel $K_{snow}(\theta, \vartheta, \varphi)$ is modelled to represent the surface reflectance for a layer of semi-infinite, weakly absorbing, plane parallel, turbid media (Jiao et al., 2019). Under this assumption, $K_{snow}(\theta, \vartheta, \varphi)$ is given by,

$$K_{snow}(\theta, \vartheta, \varphi) = R_0(\theta, \vartheta, \varphi)(1 - \alpha \cdot cos\xi \cdot exp(-cos\xi)) + 0.4076\alpha - 1.1081, \quad (3)$$

where $R_0(\theta, \vartheta, \varphi)$ is the surface reflectance at zero absorption,

$$R_0(\theta, \vartheta, \varphi) = \frac{K_1 + K_2(cos(\theta) + cos(\vartheta)) + K_3 cos(\theta) \cdot cos(\vartheta) + P(\xi)}{4(cos(\theta) + cos(\vartheta))}, \quad (4)$$

and

$$P(\xi) = 11.1e^{-0.087(180-\xi)} + 1.1e^{-0.014(180-\xi)}, \quad (5)$$

where $K_1 = 1.247$, $K_2 = 1.186$, $K_3 = 5.157$, and ξ is the phase angle (in degrees). It is important to note that all angle calculations are conducted in radians, except for ξ, which is in degrees and is calculated as follows,

$$cos(\xi) = sin(\theta)sin(\vartheta)cos(\varphi) + cos(\theta)cos(\vartheta). \quad (6)$$

Furthermore, α is a correction parameter intended to alleviate modelling errors of snow forward-scattering under large view zenith

angles (>60°), and it is defined as 0.3 based on a sensitivity analysis performed by Jiao et al. (2019).

The parameters $f_{iso}(\lambda)$, $f_{vol}(\lambda)$, $f_{geo}(\lambda)$, and $f_{snow}(\lambda)$ are retrieved by solving a weighted linear equation system. These parameters are the system's unknowns that are multiplied by each kernel, resulting in the observed MODIS (Terra satellite MOD09GA product) surface reflectance. The number of equations in the system is equal to the number of available MOD09GA observations within the 16-day window. The kernels and observations were weighted by the percentage of the grid cell area covered by each observation and by the temporal distance from the day of interest. A Laplace distribution was used for the temporal weights in which the weights vary from 0.5 (farthest day) to 1 (day of interest), following Wang et al. (2018). The parameters were retrieved by attempting to minimize the least-squares error between the observed MOD09GA surface reflectance $\rho(\theta, \vartheta, \varphi, \lambda)$ and the BRDF reflectance $R(\theta, \vartheta, \varphi, \lambda)_v$ or $R(\theta, \vartheta, \varphi, \lambda)_s$, modelled using the approach described in Eqs. (1)–(6), inside a 16-day window. The weighted linear least-squares method was constrained to only allow for the retrieval of positive parameters, following Lewis (1995). The same retrieval period of the MODIS operational product (16 days) is used. This window is defined to provide enough pixels for the retrieval to succeed, and in most cases, cloud cover occurs on multiple days within that period. The output is an image for each parameter at a MODIS 500 m spatial resolution for a specific date (the 9th day of the 16 days): $f_{iso}(\lambda)$, $f_{vol}(\lambda)$, $f_{geo}(\lambda)$, and $f_{snow}(\lambda)$. Note that the MOD09GA surface reflectance was corrected to resemble a reflectance that would have been observed with Sentinel-2A and 2B's spectral response following Pearlman et al. (2003) and Scarino et al. (2016). More information on the correction of spectral response between MODIS-Terra and Sentinel-2A and 2B can be found in Appendix A. MOD09GA surface reflectance was also corrected to alleviate topographic effects using the Sun-Canopy-Sensor + C method following Soenen et al. (2005). This correction was made to have both MODIS and Sentinel-2 images at the same surface reflectance flat-surface reference. Both the RTLSR and the snow kernel approaches were tested for the ability to retrieve BRDF within the study area and period. The addition of the snow kernel to an operational framework to retrieve BRDF has not been addressed in previous studies.

2.4. BRDF quality control

The MODIS BRDF parameter retrieval quality control can be divided into three main steps. First, a minimum of five observations, one extra observation per number of parameters (f_{iso}, f_{vol}, f_{geo}, and f_{snow}), was required to retrieve the BRDF parameters and make sure the linear system is overdetermined (Verstraete et al., 1996; Wang et al., 2007). A minimum of four observations was adopted for the RTLSR model. The retrieval of parameters with a number of observations lower than 7 was allowed, as long as it passed the thresholds of the next step, which ensure that sufficient angular information is available for a successful model inversion. Second, the RMSE and Weight of Determination (WoD) were calculated and used to remove pixels that did not meet certain thresholds. The thresholds used were 0.08, 1.65, and 2.50 for RMSE, WoD of directional-hemispherical reflectance at nadir and 45° solar angle (WoD-WDR), and WoD of bi-hemispherical reflectance (WoD-WSA), respectively, as recommended by Shuai et al., 2008. RMSE and WoD-WDR were calculated for directional reflectances using the angular information of available observations inside the 16-day window. Third, if more than 50% of the BRDF retrieval AOI pixels did not pass step 2's threshold, the high spatial resolution albedo processing was interrupted. This last step is necessary to make sure that enough pixels are available to calculate the AN ratio and transfer enough BRDF information to the high spatial resolution pixels. The R^2 was also retrieved for comparison with other studies. The R^2 was computed from the relationship between the MODIS surface reflectance and the surface reflectance modelled using the retrieved BRDF parameters for the same MODIS observation geometry inside the 16-day window. The quality control metrics for the

RTLSR and snow kernel models were compared, and the best model was used to proceed with the high spatial resolution albedo retrieval.

2.5. Retrieval of Albedo-to-Nadir ratios

It is necessary to calculate three sets of reflectance to retrieve blue-sky albedo at a Sentinel-2 spatial resolution. These are all calculated at a MODIS spatial resolution of 500 m, as f_{iso}, f_{vol}, f_{geo}, and f_{snow} are calculated using its surface reflectance. First, $R(\theta, \vartheta, \varphi, \lambda)_s$ is calculated using viewing and illumination angles from Sentinel-2, as given by Eqs. (2)–(6). These angles are available at Sentinel-2 XML metadata at a 5 km spatial resolution, but they are resampled to the MODIS resolution using bilinear interpolation. Note that hereinafter each kernel will be represented by the subscript k and that the calculation of $R(\theta, \vartheta, \varphi, \lambda)_v$ is the same as for $R(\theta, \vartheta, \varphi, \lambda)_s$, but without the $f_{snow}(\lambda)K_{snow}(\theta, \vartheta, \varphi)$ term. Second, the BRDF reflectance integrated in the view zenith and relative azimuthal angles is calculated by integrating each kernel $K_k(\theta, \vartheta, \varphi)$ to further generate black-sky albedo $R_{bs}(\theta, \lambda)$,

$$h_k(\theta) = \frac{1}{\pi} \int_0^{2\pi} \int_0^{\pi/2} K_k(\theta, \vartheta, \varphi) \sin(\vartheta)\cos(\vartheta) d\vartheta d\varphi, \quad (7)$$

$$R_{bs}(\theta, \lambda) = f_{iso}(\lambda) + h_{vol}(\theta) \cdot f_{vol}(\lambda) + h_{geo}(\theta) \cdot f_{geo}(\lambda) + h_{snow}(\theta) \cdot f_{snow}(\lambda). \quad (8)$$

Third, each $K_k(\theta, \vartheta, \varphi)$ kernel is integrated in the solar, view zenith, and relative azimuthal angles to further generate white-sky albedo $R_{ws}(\lambda)$ (Lucht et al., 2000),

$$H_k = \frac{2}{\pi} \int_0^{\pi/2} \int_0^{2\pi} \int_0^{\pi/2} (K_k(\theta, \vartheta, \varphi) \sin(\vartheta)\cos(\vartheta)) \sin(\theta)\cos(\theta) d\vartheta d\varphi d\theta, \quad (9)$$

$$R_{ws}(\lambda) = f_{iso}(\lambda) + H_{vol} \cdot f_{vol}(\lambda) + H_{geo} \cdot f_{geo}(\lambda) + H_{snow} \cdot f_{snow}(\lambda). \quad (10)$$

Following calculation of these radiometric quantities, the Albedo-to-Nadir (AN) ratios for black-sky $a_{bs}(\theta, \lambda)$ and white-sky $a_{ws}(\lambda)$ albedo can be calculated (Shuai et al., 2011),

$$a_{bs}(\theta, \lambda) = R_{bs}(\theta, \lambda) / R(\theta, \vartheta, \varphi, \lambda)_s, \quad (11)$$

$$a_{ws}(\lambda) = R_{ws}(\lambda) / R(\theta, \vartheta, \varphi, \lambda)_s. \quad (12)$$

2.6. Sentinel-2 image processing

Prior to conducting the processing to retrieve high spatial resolution albedos, it was necessary to correct the Sentinel-2 TOA reflectance for atmospheric attenuation and scattering. Sentinel-2 TOA reflectance images, with less than 30% cloud-shadow coverage within the MODIS sampling AOI shown in Fig. 1 for the study period, were selected using a Google Earth Engine (GEE) cloud-shadow screening. GEE was used to identify the image ID that was later downloaded from the Sentinel-2 Copernicus website (https://scihub.copernicus.eu/). Table 2 shows the

Table 2
Number of available Sentinel-2 images, number of selected images by the cloud-shadow screening, and the characteristics of each year.

Year	# Available Images	# Images < 30%	Characteristics
2016	7	1	Reduced fire activity and no Sentinel-2B images
2017	15	5	Active fire season throughout the summer months
2018	30	8[1]	Active fire season concentrated in August
2019	29	3	Reduced fire activity
2020	30	7	Smoke present in season's last 3 days

[1] There was <30% cloud-shadow cover in the image of 2018-08-18; however, it was covered by visually identified dense smoke for the majority of the MODIS sampling AOI, and it was thus not considered in this study.

images available for the study and certain associated characteristics for each year. In this respect, there was reduced wildfire activity in 2016, 2019, and 2020, but there were intense wildfire seasons in 2017 (throughout all summer months) and 2018 (concentrated in August). To define cloud clover (cloud probability >50%), the GEE cloud-shadow screening method uses the Sentinel-2 Cloud Probability Collection, generated from the s2cloudless algorithm (https://github.com/sentinel-hub/sentinel2-cloud-detector), and identifies cloud shadows based on low near-infrared (NIR) reflectance values searched in a 1.5 km projection distance from the cloud edge. An additional 100 m buffer was added to the cloud-shadow mask to avoid edge effects. More information about the cloud-shadow screening algorithm can be found at https://developers.google.com/earth-engine/tutorials/community/sentinel-2-s2cloudless.

The Sentinel-2 images were downloaded as TOA reflectance and were further atmospherically corrected using the Sen2Cor v2.8 model (Mueller-Wilm et al., 2019). In Sen2Cor parameterization, the ozone concentration was set automatically using the ozone concentration obtained from auxiliary data, and the best LUT that described the concentration was then searched for. The best aerosol LUT was also determined automatically, in which the algorithm calculates the path radiance for different aerosol loads in the blue and red bands and compares it to dark invariant pixels, which are typically forested vegetation. A correction for water vapor (WV) absorption was also applied. This correction compares the retrievals from the 864 nm band (region of low WV absorption) to the 945 nm band (region of high WV absorption) and corrects the radiance based on that difference. Furthermore, cirrus influence was corrected using information from the 1373 nm band. The Sentinel-2 surface reflectance was also corrected for topographic effects during the atmospheric correction process. Sen2Cor v2.8 performs a Minnaert-like topographic correction on the surface reflectance that increases the reflectance in faintly illuminated sloped terrain. A b exponent of 0.5 was adopted for the topographic correction following Mueller-Wilm et al. (2019).

2.7. Retrieval of Sentinel-2 blue-sky albedo

The AN ratio was calculated using MODIS imagery only. These ratios were then applied to Sentinel-2 surface reflectance $\rho_{S2}(\theta, \vartheta, \varphi, \lambda)$ for the retrieval of black-sky $\alpha_{bsa}(\theta, \lambda)$ and white-sky $\alpha_{wsa}(\lambda)$ spectral albedos at a 20 m spatial resolution, following the method of Shuai et al. (2011) and Li et al. (2018). This method assumes that spectral similarity between coarse and fine resolution homogenous pixels can be translated into BRDF similarity. Therefore, spectral Sentinel-2 surface reflectance was used to retrieve albedo at a finer spatial resolution, assuming that the albedo to nadir variation is similar for spectrally homogenous surfaces inside a MODIS pixel. A cluster surface classification is utilized to define the degree of homogeneity inside a MODIS pixel. This classification needs to be performed using the six bands of the reflective spectrum of Sentinel-2, in which the ratio is only sampled from MODIS when a respective Sentinel-2 cluster class covers more than 60% of a MODIS pixel.

As the number of cluster classes for surface classification can be a sensitive parameter, it was defined based on the observed albedo at the Athabasca Glacier AWS. The associated sensitivity is caused mostly by the temporal variability of reflectance, which is high in icefields as they respond to snowfall, melt, and soot deposition events. The optimal number of classes was therefore determined every 15 days by considering from 6 to 20 cluster classes, optimised using the albedo RMSE. The five 15-day periods between Jul. 1 and Sept. 15 would yield five different numbers of cluster classes. For example, at the first iteration, the number of cluster classes was set to 6, 7, 8, 9, and 10 for images within the Jul. 1–15, Jul. 16–31, Aug. 1–15, Aug. 16–31, and Sept. 1–15 periods, respectively, and the RMSE between the Sentinel-2 and Athabasca Glacier AWS albedo was calculated. At the next iteration, the number of cluster classes was set to 7, 8, 9, 10, and 11, and the RMSE

was calculated again. This process was repeated until the RMSE for all combinations of cluster numbers for the five periods was calculated. The cluster number with the smallest RMSE was used to represent the number of cluster classes for each 15-day period (Fig. 3). The remote sensing Sentinel-2 albedos used for the number of cluster classes sensitivity analysis and evaluation are a direct extraction from the pixel at the Athabasca Glacier AWS, and the majority of the upwelling shortwave radiometer field of view is bounded by this pixel (Fig. 1).

The AN ratio was sampled for each of these classes by extracting the mean of all >60% MODIS pixels for black-sky $\bar{a}_{bs}(\theta, \lambda)$ and white-sky $\bar{a}_{ws}(\lambda)$ albedos, and it was applied to the Sentinel-2 pixels classified as the respective cluster class as follows,

$$S2_{bsa}(\theta, \lambda) = \bar{a}_{bs}(\theta, \lambda) \cdot \rho_{S2}(\theta, \vartheta, \varphi, \lambda), \qquad (13)$$

$$S2_{wsa}(\lambda) = \bar{a}_{ws}(\lambda) \cdot \rho_{S2}(\theta, \vartheta, \varphi, \lambda). \qquad (14)$$

To focus on the albedo over snow and ice, a mask with a normalized difference snow index (NDSI) higher than 0.4,

$$NDSI = \frac{\rho_{S2}(559 \, nm) - \rho_{S2}(1,610 \, nm)}{\rho_{S2}(559 \, nm) + \rho_{S2}(1,610 \, nm)}, \qquad (15)$$

and a reflectance at $\rho_{S2}(559 \, nm) > 0.1$ (Klein et al., 1998), was created. For the narrow-to-broadband conversion, the coefficients developed by Li et al. (2018) for Sentinel-2 and snow-covered surfaces were used as follows,

$$\alpha_{bsa}(\theta) = -0.0001 - 0.1992 \cdot S2_{bsa}(492 \, nm) + 2.3002 \cdot S2_{bsa}(559 \, nm)$$
$$- 1.9121 \cdot S2_{bsa}(665 \, nm) + 0.6715 \cdot S2_{bsa}(864 \, nm) \qquad (16)$$
$$- 2.2728 \cdot S2_{bsa}(1,610 \, nm) + 1.9341 \cdot S2_{bsa}(2,186 \, nm).$$

It is also of note that the central wavelength varies slightly between the two satellites, Sentinel-2A and 2B, but the same narrow-to-broadband coefficients were used. White-sky albedo, α_{wsa}, was calculated similarly, but using $S2_{wsa}(\lambda)$ spectral white-sky albedos. The Sentinel-2 blue-sky albedo, α_{blue}, was linearly interpolated between $\alpha_{bsa}(\theta)$ and α_{wsa} by computing the ratio between diffuse and total shortwave irradiance $SKY(\theta)$, using observations from the Athabasca Glacier AWS,

$$\alpha_{blue}(\theta) = (1 - SKY(\theta)) \cdot \alpha_{bsa}(\theta) + SKY(\theta) \cdot \alpha_{wsa}, \qquad (17)$$

where $SKY(\theta)$ was calculated following Ellis and Pomeroy (2007) as

$$SKY(\theta) = 1.1 - 1.09k_T, \qquad (18)$$

and k_T was calculated as the ratio between the measured shortwave irradiance and the modelled TOA shortwave irradiance at 13:00:00 central standard time (CST) for a specific date (Ellis and Pomeroy, 2007). Finally, albedos higher than one and lower than zero were not considered in the analysis.
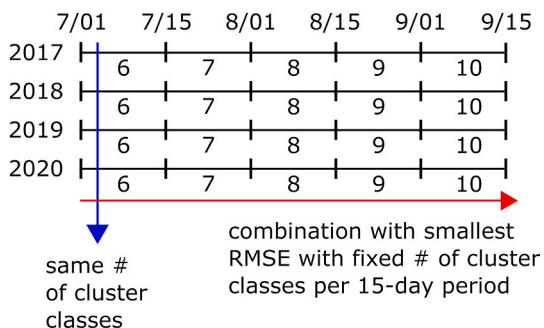

Fig. 3. Example of the number of cluster classes selection strategy. Each row is a year and each column is a 15-day period.

2.8. Net shortwave radiation

Positive K* is defined here as the amount of shortwave radiation entering the surface of snow and ice, and it was retrieved using measured shortwave irradiance at the Athabasca Glacier AWS at the nearest available 15-min measurement from Sentinel-2 overpass time. The total shortwave irradiance at the station was extrapolated for the entire Columbia Icefield utilizing the Sentinel-2 albedo and Allen et al. (2006) method to correct for slope and aspect, resulting in the K*. Slope and aspect was calculated from the SRTM 30 m digital elevation model. Spatial extrapolation was based on the assumption that there would be no considerable change in atmospheric attenuation to the surface between the elevation of the AWS (2177 m a.m.s.l.) and higher elevations within the Columbia Icefield (~ 3700 m a.m.s.l.). The AWS measured air temperature and relative humidity used in the K* method were also taken at the nearest available 15-min measurement from Sentinel-2 overpass time. The slope and aspect correction method of Allen et al. (2006) used here employs a multiplicative factor (f) that enhances or diminishes observed irradiance. The f factor is 1 when the slope and aspect do not influence irradiance, and less or more than 1 when this influence decreases or increases, respectively. The f factor is a function of direct (f_B), diffuse (f_{ia}), and reflected radiation (f_i). The turbidity coefficient (K_t) from Allen et al. (2006) was set to 0.75 when smoke was identified by the timelapse camera; otherwise, the coefficient was set to 1. To compute spatial averages, the Columbia Icefield was discretized into the high-elevation snow plateau, northeast-facing, southwest-facing, and southeast-facing glaciers (Fig. 1). Further discretization into low ($\leq 16°$) and high ($> 16°$) slope glaciers was applied to analyze the effects of slope and aspect on K*. The number of cumulative smoky days (CSD) shown in Table 4 was used as a proxy for known upwind fire activity, and it was defined by supervised visual classification of three photos taken per day by the timelapse camera and confirmed by visual observations in the field. A day is considered smoky when any of the three photos have light or dense smoke, and CSD were accumulated continuously during the five analyzed summers.

3. Results and discussion

3.1. BRDF modelling evaluation

The comparison between the RTLSR and the snow kernel BRDF models revealed that, although the mean RMSE is slightly better for the RTLSR (RTLSR: 0.047, snow: 0.049, and t-test p-value: 0.6186) and the mean R^2 is slightly better for the snow kernel (RTLSR: 0.80, snow: 0.82, and t-test p-value: 0.0732), the differences between their means are not statistically significant. This represents that in terms of RMSE and R^2 there is not a statistically significant difference between using the RTLSR and the snow kernel to model BRDF in this region. On the other hand, the WoD-WDR and WoD-WSA metrics were one to three orders of magnitudes higher for the snow kernel. Only two dates had a mean WoD-WDR within the thresholds recommended by Shuai et al. (2008), and no date was able to meet the WoD-WSA thresholds for the snow kernel model (Fig. 4). The WoD-WDR (RTLSR: 0.371, snow: 23.589, and t-test p-value: 0.0118) and WoD-WSA (RTLSR: 3.948, snow: 593.716, and t-test p-value: 0.0001) means difference were statistically significant in this case. The snow kernel model has not yet been applied in an operational framework that relies on limited satellite/sensor angular sampling, only in situations in which ample angular information was available (Jiao et al., 2019). There are most likely two factors at play for the increased snow kernel BRDF estimates uncertainty. First, using the snow kernel implies that the minimum number of observations needs to be higher once one kernel is added to the RTLSR BRDF model, and the WoDs are sensitive to the number of observations (Lucht and Lewis, 2000). This can be particularly important in an already data-scarce region due to high cloud cover frequency. Second, it is possible that the addition of the snow kernel to the BRDF model under the available
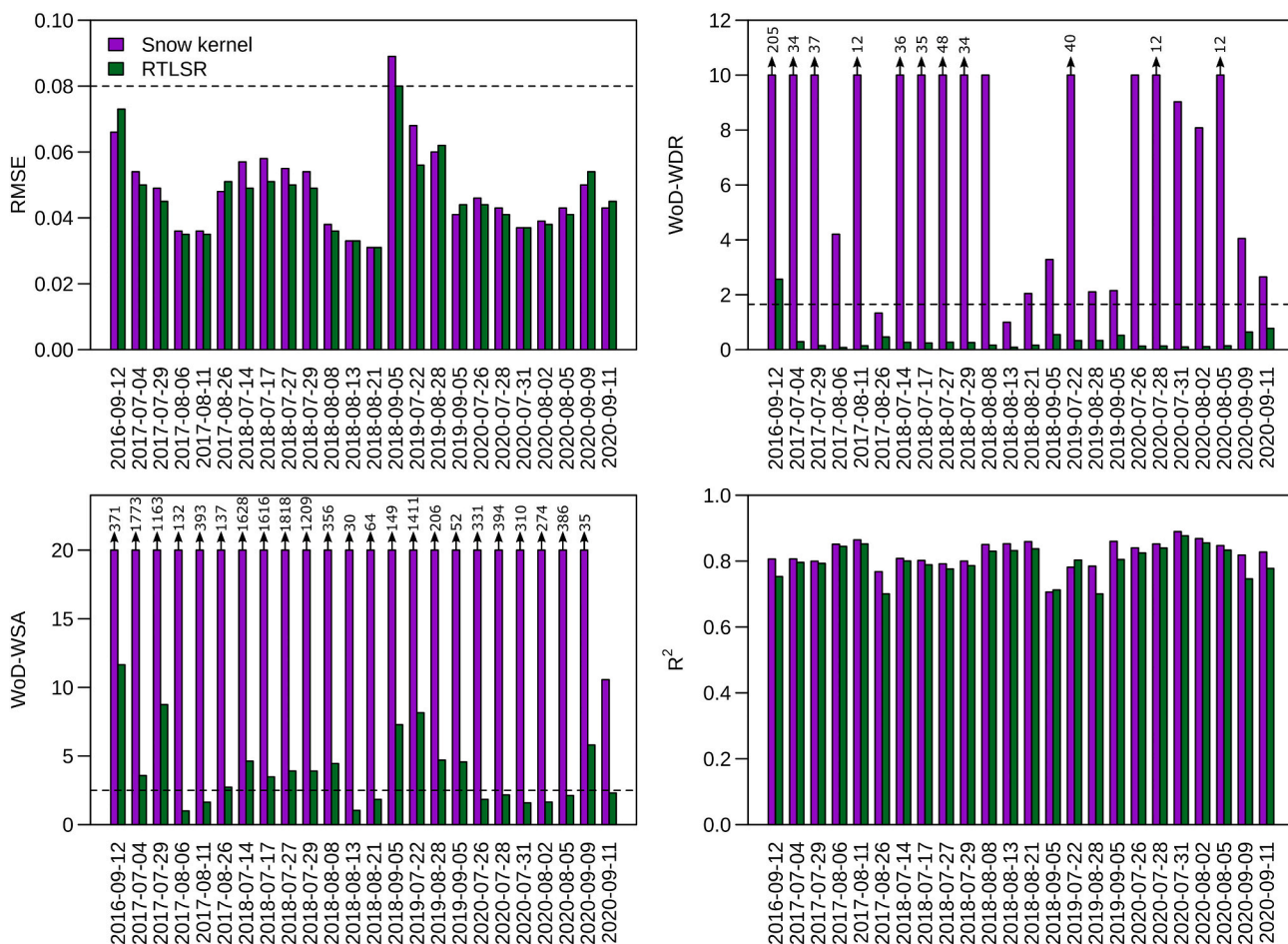
Fig. 4. Comparison between the ability of the snow kernel and RTLSR approaches to model the BRDF of the study area. The evaluation metrics RMSE, WoD-WDR, WoD-WSA, and R^2 are presented as the average of all 6 MODIS bands for each date. QC non-compliant pixels are also included in calculating the averages. The R^2 was calculated by comparing MODIS observed and modelled surface reflectance inside the 16-day windows. The dashed lines are the thresholds determined by Shuai et al. (2008). The WoD-WDR and WoD-WSA plots are cutoff at 10 and 20, respectively, to observe the RTLSR values. The arrows indicate that the bars continue to increase until the values above them.

angular sampling introduces excessive random noise to be able to reliably retrieve the BRDF parameters (Lucht and Lewis, 2000). Given the above evaluation metrics and the inability of the snow kernel to generate high quality BRDF pixels in terms of WoDs, the RTLSR BRDF model was adopted to retrieve high spatial resolution albedo, as it has already been employed with satisfactory results over snow and ice (Li et al., 2018; Mortimer and Sharp, 2018; Wang et al., 2016).

Table 3 shows the results of the MODIS RTLSR BRDF modelling evaluation. The values of Table 3 are the mean for all the 6 MODIS bands. The RMSE remained below or equal to 0.08 for all the 24 BRDF estimates; however, both WoD-WDR and WoD-WSA have exhibited estimates that had insufficient angular information for a successful $f_k(\lambda)$ parameter retrieval. These dates had average WoD values that surpassed the thresholds recommended by Shuai et al. (2008). Table 3 and Fig. 5 show that by removing pixels that surpassed the quality control criteria for RMSE, WoD-WDR, and WoD-WSA of 0.08, 1.65, and 2.50, respectively, some BRDF estimates became unusable for the high spatial resolution albedo estimation. In contrast, 2017-08-26 and 2019-09-05 could still cover more than 50% of the MODIS BRDF AOI, even presenting a mean WoD-WSA above the threshold, and thus, were kept for high spatial resolution albedo estimation.

In general, late-spring and early-fall BRDF estimates presented a lower number of high quality pixels that could be used for high spatial resolution albedo estimation. This decrease in BRDF retrieval quality happens because cold temperatures are more prominent during these

periods, increasing cloud-cover and reducing the amount of MOD09GA surface reflectance observations. Previous studies have resolved cloud cover limitations by adopting a minimum of seven observations per pixel to produce a BRDF estimate (e.g., Roy et al., 2008; Schaaf et al., 2002); however, this restriction was not followed to avoid missing any reasonable retrievals, which could occur when using fewer than seven observations. Adopting the latter approach is particularly important in mountain regions where orographic lift contributes to cloud formation and increases cloud-cover frequency (Da Ronco and De Michele, 2014). Retrieving a BRDF estimate with less than 7 observations was also performed to preserve the semi-empirical nature of the BRDF retrievals (Schaaf et al., 2002), which is important for capturing changes in the anisotropy of snow and ice due to wildfire soot deposition, rather than using a magnitude inversion (empirical), as seen in the MODIS operational product (Strugnell and Lucht, 2001). It is worth mentioning that the WoDs were calculated to ensure sufficient angular information was present to retrieve the BRDF parameters with a minimum of 4 observations.

BRDF reflectance modelling from MODIS using the RTLSR approach yielded a mean $R^2 \geq 0.65$ for all bands. However, there was some difference between the highest mean R^2 values from the visible, NIR, and shortwave infrared (SWIR) bands, 0.87, 0.82, and 0.69, respectively (Fig. 4). These R^2 values show that the quality of the BRDF estimates decreases with the band wavelength size, but still provides reasonably good results for the SWIR bands. The higher uncertainty can be related

Table 3

RTLSR BRDF model evaluation metrics RMSE, WoD-WDR, WoD-WSA, R^2, and percentage of pixels excluded by the quality control method inside the BRDF sampling AOI (% QC NA). All the metrics are presented as the average of all 6 MODIS bands for each date. QC non-compliant pixels are also included in calculating the averages.

Date	RMSE	WoD-WDR	WoD-WSA	R^2	% QC NA
2016-09-12	0.073	2.565	11.647	0.75	74.0
2017-07-04	0.050	0.290	3.576	0.80	68.1
2017-07-29	0.045	0.147	8.746	0.79	61.0
2017-08-06	0.035	0.077	1.002	0.84	13.4
2017-08-11	0.035	0.142	1.633	0.85	17.0
2017-08-26	0.051	0.461	2.727	0.70	42.9
2018-07-14	0.049	0.267	4.624	0.80	88.1
2018-07-17	0.051	0.243	3.480	0.79	69.5
2018-07-27	0.050	0.270	3.907	0.78	64.3
2018-07-29	0.049	0.257	3.904	0.79	63.6
2018-08-08	0.036	0.166	4.453	0.83	82.2
2018-08-13	0.033	0.085	1.037	0.83	5.3
2018-08-21	0.031	0.164	1.840	0.84	16.8
2018-09-05	0.080	0.548	7.279	0.71	90.0
2019-07-22	0.056	0.332	8.151	0.80	61.4
2019-08-28	0.062	0.334	4.702	0.70	83.6
2019-09-05	0.044	0.522	4.567	0.80	49.3
2020-07-26	0.044	0.128	1.841	0.82	27.0
2020-07-28	0.041	0.132	2.165	0.84	39.8
2020-07-31	0.037	0.101	1.588	0.88	12.8
2020-08-02	0.038	0.108	1.645	0.86	15.5
2020-08-05	0.041	0.140	2.120	0.83	33.2
2020-09-09	0.054	0.641	5.803	0.75	57.6
2020-09-11	0.045	0.774	2.307	0.78	32.7

to the SWIR bands' spectral albedo higher sensitivity to snow grain size (Gardner and Sharp, 2010). Nonetheless, the lower SWIR quality seems to not have an impact on the high spatial resolution albedo retrievals for the purpose of this study, as reflectance beyond NIR is not affected by soot deposition (Gardner and Sharp, 2010; McKenzie Skiles et al., 2018).

3.2. Albedo retrieval evaluation

The cloud-shadow screening algorithm provided good results for 20 out of the 24 retrievals. However, on four occasions, the cloud-shadow screening algorithm failed: three times in relation to shadows over snow and once due to a thin cloud. The former occasions were corrected using a directional buffer opposed to the sun azimuth to mask visually identified cloud shadows over snow, and the latter occasion was corrected using a simple buffer until the thin cloud was completely masked out of the Columbia Icefield. The original and modified cloud-shadow masks for the four occasions are presented in Appendix B.

In previous studies, the number of cluster classes used for unsupervised classification was determined arbitrarily from 10 to 20 classes (Li et al., 2018; Shuai et al., 2011). However, Shuai et al. (2011) indicated that this parameter could be sensitive to the final Sentinel-2 albedo retrieval, and we also found this here to a certain degree. Therefore, a procedure was conducted to determine the most suitable number of cluster classes. The high spatial resolution part of the albedo retrieval algorithm was run multiple times with the number of cluster classes varying from six (the number of bands used in the cluster classification) to 20. To the authors' knowledge, this procedure has not yet been employed by any of the high spatial resolution albedo studies. Fig. 6 shows the sensitivity of albedo retrieval to the number of cluster classes, together with the Athabasca Glacier AWS observed albedo and the albedo value for the selected number of cluster classes. It is worth noting that since the BRDF quality control excluded half of the high spatial resolution images, only 12 images are shown hereinafter. The results show that the sensitivity of albedo to the number of cluster classes generally did not exceed 0.05, except for 2018-08-21. This date's increased sensitivity is most likely related to the degree of aerosols in the atmosphere, as this was the haziest date within the high spatial

resolution images. The identified sensitivity suggests that adopting a 15-day period number of cluster classes is generally sufficient for representing the spatiotemporal variability of reflectance, and the four 15-day period numbers of cluster classes selected by the iterative process were 17, 13, 20, and 14 (also shown in Table 4). Note that although 20 cluster classes was selected for the Aug. 15 to 31 period, this value might not be representative enough since this number has been selected solely by the image with the lowest deviation from the 2018-08-21 site-measured albedo. In addition, no image was available for the Jul. 1 to 15 period.

Fig. 7 shows a scatterplot of the evaluation of albedo retrieval using the number of cluster classes selected by the iterative process. The retrievals explained 68% of the Athabasca Glacier AWS albedo variability, with a p-value of 0.0033, bias of 0.019, and RMSE of 0.026. These evaluation statistics compare well with other high spatial resolution remote sensing albedo studies that found an R^2 value of 0.78 (Shuai et al., 2011) and bias and RMSE values ranging from −0.029 to 0.001 and 0.025 to 0.043 (Li et al., 2018; Shuai et al., 2011; Wang et al., 2016), respectively. Most likely the 32% variability in site-measured albedo that is not explained by the high spatial resolution estimates is caused by spatial representativeness errors due to the difference in footprint size between the Athabasca Glacier AWS albedometer (110 m^2) and the Sentinel-2 pixel (400 m^2), and the low number of observations. Clearly, the remote sensing albedo retrieved on 2018-08-21 (isolated point on the scatterplot's upper right corner) is exerting a strong influence in the calculated R^2. It is worth mentioning that the scatterplot and statistics were computed without 2017-08-26 and 2018-08-13 because the AWS was not operating and because the cloud-shadow screening removed the image area where the Athabasca Glacier AWS is located, respectively, totalling 10 data pairs. These findings also show that the BRDF model employed in this study provides a good representation of the spatiotemporal variation of albedo in this high-elevation icefield.

3.3. Sentinel-2 blue-sky albedo retrievals

Given the scarcity of high spatial resolution albedo estimates, the inter-annual comparisons of albedo and K* were made by matching one image of each soot-impacted year (2017, 2018, and 2019) with the closest day of the year image of 2020. The selected dates are 2017-08-06 and 2020-08-05; 2018-08-13 and 2020-08-05; and 2019-09-05 and 2020-09-11. This assumption is reasonable since it is considered that the differences between years impacted (2017, 2018, and 2019) and a control year not impacted by soot deposition, which in this case is 2020, can be attributed to soot deposition, apart from fresh snowfall. Therefore, this analysis focussed on changes between the control year and the minimum albedo and maximum K* encountered during the 2017, 2018, and 2019 years. The albedo and K* minima and maxima will still be retrieved from all the 12 high spatial resolution images, except for 2018-08-21, since the bias for this image is large.

Fig. 8 only shows the images used for inter-annual comparisons for a better visual analysis. The lowest snow albedo (0.4 to 0.5) was observed in 2018 for the plateau's southern section; however, the plateau was superimposed by a layer of high albedo snow cover (0.6 to 0.9) due to fresh snowfall in the northern higher elevations. A layer of fresh snowfall was also present in 2019, but the remaining low albedos are of intermediate values (0.5 to 0.6), as was the case for the entire plateau in 2017. Snow albedo recovered to 0.6 to 0.7 values in 2020, which appear to be more spatially homogeneous within the plateau. Glacier albedos were the lowest in 2018 and 2019, with widespread values <0.2. Glacier albedos between 0.3 and 0.4 became more frequent in 2020, and more incursions of the snowline into the glacier boundaries also indicate an overall albedo increase. The albedo spatial variability demonstrated in Fig. 8 reinforces the need to use high spatial resolution albedo to determine snow and ice energetics and further hydrological applications. Coarse resolution remote sensing and modelling would not be able to properly reproduce this spatial variability. Although the timeseries of
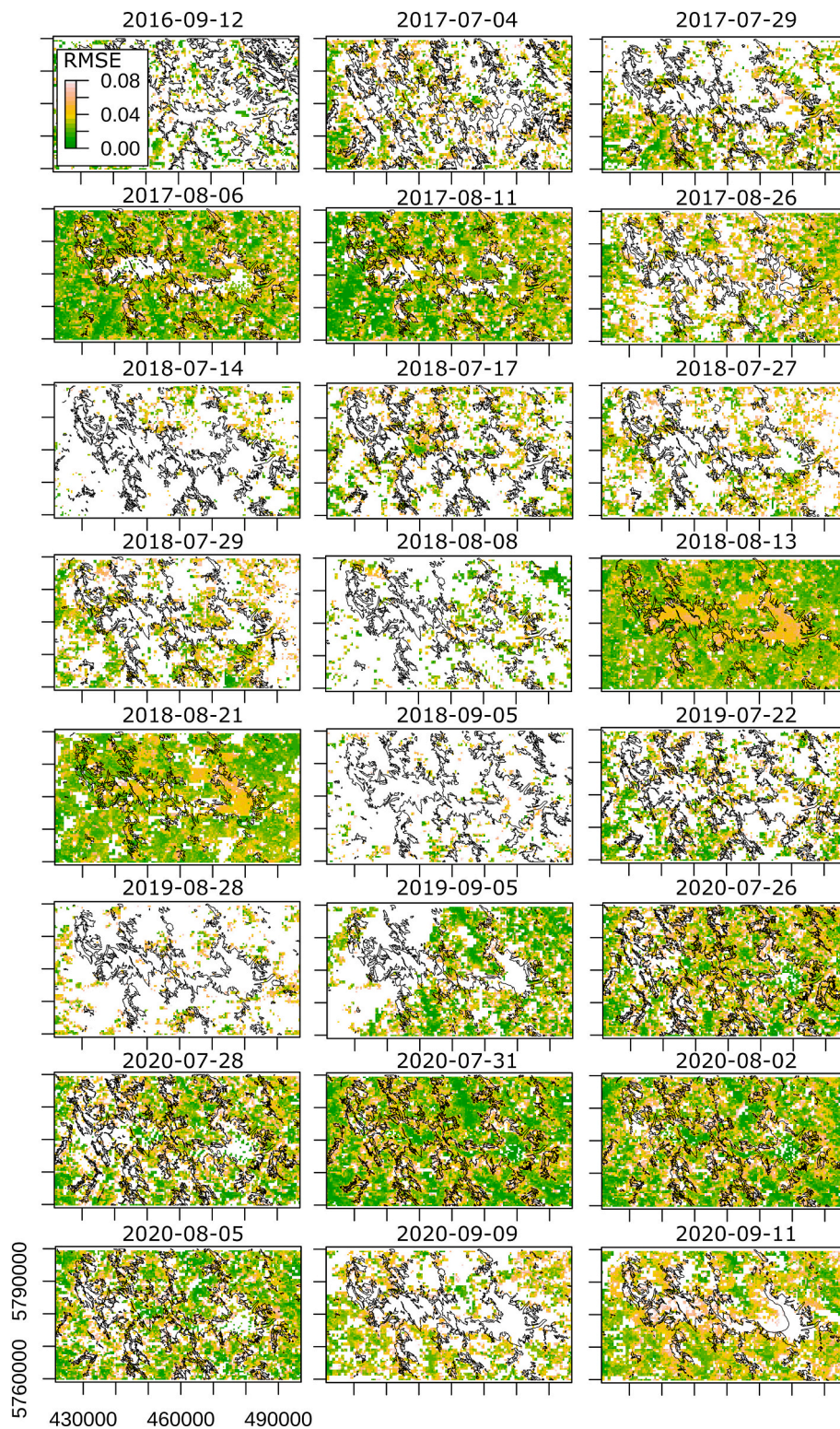
Fig. 5. MODIS RTLSR BRDF RMSE maps with the Sentinel-2 snow and ice cover displayed in the black lines. The snow and ice polygons were simplified for clarity. White spaces are pixels that did not pass the BRDF quality control.

observed and remote sensing albedo demonstrate that the retrievals represent the temporal variation of albedo reasonably well, there is a small positive bias in the remote sensing retrievals (Fig. 9). This bias is substantially exacerbated on 2018-08-21. The presence of light smoke was observed by the timelapse camera during 2018-08-21, and it appears to greatly influence this albedo retrieval. Another evidence of poor

retrieval for 2018-08-21 is that the cloud-shadow screening algorithm mistakenly identified light smoke over the edges of the Athabasca and Saskatchewan glaciers as thin clouds; these pixels were excluded from the analysis.

Although these results are able to represent high spatial resolution albedo properly in this complex environment, there are some limitations
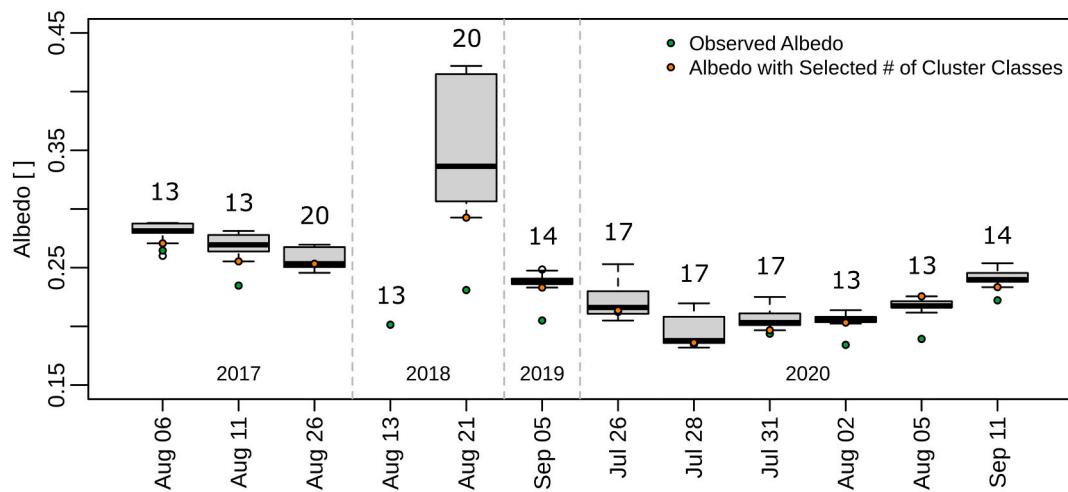
Fig. 6. Sensitivity to the number of cluster classes. Each boxplot represents the albedo values at the Athabasca Glacier AWS pixel calculated with a number of cluster classes varying from 6 to 20. The green and orange points represent the Athabasca Glacier AWS observed albedo and the pixel albedo value for the selected number of cluster classes, respectively. The selected number of cluster classes is labelled above each boxplot. (For interpretation of the references to colour in this figure legend, the reader is referred to the web version of this article.)

Table 4
Sentinel-2 image IDs, cloud-shadow cover inside the BRDF sampling AOI (%), number of classes from cluster surface classification, CSD (inclusive), prior 48-h precipitation at Athabasca Moraine AWS, and precipitation phase if snowfall occurred (R: rain and S: snow).

Sentinel-2 Image ID	Cloud-shad. cover	# cluster classes	CSD	48-h precip. (mm)	Precip. phase R/S (mm)
20160912T184952_20160912T185015_T11UMT	3.87	–	0	12.68	11.423/1.253
20170704T184919_20170704T185934_T11UMT	15.39	–	0	0	–
20170729T184921_20170729T185816_T11UMT	3.37	–	7	0	–
20170806T185919_20170806T190802_T11UMT	2.03	13	10	0	–
20170811T185921_20170811T190305_T11UMT	0.13	13	12	0	–
20170826T185909_20170826T190150_T11UMT	8.68	20	17	0.67	–
20180714T184921_20180714T185034_T11UMT	22.12	–	25	8.12	–
20180717T185921_20180717T185917_T11UMT	0.12	–	25	0	–
20180727T185921_20180727T185917_T11UMT	25.30	–	26	0.06	–
20180729T184919_20180729T185102_T11UMT	3.53	–	27	0.14	–
20180808T184909_20180808T185846_T11UMT	0.56	–	32	0	–
20180813T184921_20180813T185918_T11UMT	29.11	13	35	22.49	–
20180821T185909_20180821T185909_T11UMT	16.67	20	43	0	–
20180905T185911_20180905T190544_T11UMT	0.45	–	47	0.27	0.254/0.018
20190722T185921_20190722T190551_T11UMT	1.16	–	48*	0.08	–
20190828T184921_20190828T185739_T11UMT	3.46	–	48	2.62	–
20190905T185919_20190905T190714_T11UMT	4.53	14	48	1.18	–
20200726T185921_20200726T190505_T11UMT	1.74	17	48	0.79	–
20200728T184919_20200728T184920_T11UMT	3.07	17	48	0	–
20200731T185919_20200731T190527_T11UMT	3.48	17	48	0	–
20200802T184921_20200802T185701_T11UMT	25.96	13	48	0.33	–
20200805T185921_20200805T190700_T11UMT	0.74	13	48	0	–
20200909T185929_20200909T190120_T11UMT	0.02	–	48	0	–
20200911T184951_20200911T185837_T11UMT	10.41	14	48	0	–

* The extra smoky day in 2019 is a result of accumulation from a smoky day after the last 2018 retrieval. There was no wildfire activity in 2019.

at sites with particularly rugged terrain and landcover heterogeneity. Since the Sentinel-2 20 m spatial heterogeneity is dampened at the MODIS 500 m pixel, scaling issues can arise. Jiao et al. (2018) have found that decreasing the resolution of BRDF estimates from POLDER to MODIS can reveal additional BRDF shapes. Román et al. (2011) have found that the uncertainty (RMSE) associated with downscaling BRDF at MODIS resolution to a 30 m resolution varies from 0.0097 to 0.1717, depending on the view zenith angle and wavelength. The present study's uncertainty due to landcover heterogeneity is expected to be smaller than that of Román et al. (2011) since their results are from a mixed agricultural landscape; however, the present study's mountain region should introduce uncertainty due to terrain heterogeneity. Schaaf et al. (1994) found that topography can cause an overestimation of the retrieved BRDF shapes for rugged terrains. Combal and Isaka (2002) have shown that even small topographic variations can introduce

change to BRDF estimates when the sun and view zenith angles are high for high (10%) and coarse (3–5%) spatial resolution imagery. The topographic correction performed using Sen2Cor v2.8 and to the MODIS surface reflectance should alleviate this issue as it converts the reflectance of rugged terrain to a flat surface.

3.4. Wildfire soot influence on snow and ice albedo and energetics

Large temporal and spatial variations in the icefield albedo are evident, as shown in Figs. 8 and 9; however, the albedo was highest for the snow plateau and lowest for the northeast-facing glaciers (Figs. 8 and 10). In addition to soot deposition, the main factors governing albedo change for the snow plateau were melt and fresh snowfall, and for glacier albedos, melt was more important. The effect of melt was also observed on the snow plateau; this area has a higher albedo at the
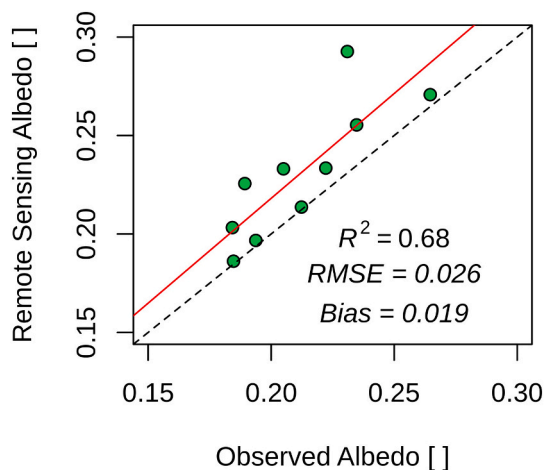
Fig. 7. Sentinel-2 blue sky albedo retrieval evaluation scatterplot between the Athabasca Glacier AWS observation and image pixel. The red and black dashed lines represent the regression fit and the 1:1 line, respectively. (For interpretation of the references to colour in this figure legend, the reader is referred to the web version of this article.)

beginning of July, but fresh snowfall can restore the snow albedo even in mid-August, as seen on 2018-08-13. The spatially-averaged snow plateau albedo was minimal (0.528) on 2017-08-11 and maximal (0.664) on 2020-07-26. The greatest recovery from soot-induced snow plateau albedo decrease was found between 2018-08-13 and 2020-08-05 from 0.556 to 0.606, respectively. Note that the albedo in 2018 could have been even lower, since the soot-induced decreased albedo values in the southern section of the plateau are in the 0.4 to 0.5 range. The increased albedo in the northern snow plateau section was due to fresh snowfall that was registered as rainfall at the Athabasca Moraine AWS (Table 4). Although fresh snowfall increased albedo in part of the snow plateau on 2018-08-13, there was still a 0.050 overall decrease caused by the remaining soot-affected area when compared with 2020-08-05. These findings highlight the rapid snow plateau albedo response to soot deposition and recovery due to fresh snowfall.

However, the influence of seasonal melt is more evident with respect to glacier surfaces, because they less frequently experience substantial summer snowfall episodes. Therefore, albedo will be at its lowest at the final retrieval of the season, unless snowfall occurs. Albedo was lowest in 2019-09-05 for NE (0.261) and SW (0.278) glaciers, and, surprisingly, in 2020-09-11 for SE glaciers (0.258). The difference from the second-lowest SE glacier albedo (2018-08-13) was only 0.004, and the albedo from 2019-09-05 (lowest for all other aspects) was not representative for this aspect due to the widespread presence of NA pixels (Fig. 8), which indicates that albedo in 2019 could have been lower than in 2020 following the trend of the remaining glaciers. Albedo was highest in 2020-07-26 for all glaciers (NE: 0.396, SE: 0.446, and SW: 0.476). All the glaciers presented the highest soot-induced albedo decrease recovery from 2018 to 2020. The highest difference in albedo (0.148) was observed for SE glaciers. Both NE and SW glaciers presented low soot-induced albedo values in 2019, even when there was no wildfire activity. These findings suggest that glacier albedo decreases during the wildfire season, but persistent low albedo is still observed the following year, even when wildfire activity ceases. This effect can be explained by bioalbedo feedback theory, in which albedo is further decreased due to glacier algae feeding on the carbon from wildfire soot deposition (Cook et al., 2020; Di Mauro et al., 2020). Algae deposited in cryoconite formations were found in field investigations in the summer of 2019 in the Athabasca Glacier (northeast). The following year, glacier albedo reached its highest levels without the occurrence of widespread summer snowfall, which suggested that it had recovered to pre-2017 levels. The albedo annual mean values from Athabasca Glacier AWS for the same

date and time of the retrievals also show similar inter-annual variabilities, but with a more modest recovery to higher albedos in 2020. It is important to note that the albedo decrease near the snow line is highly variable and dependent on each year's hydrometeorological conditions that govern melt dynamics and snowfall occurrence.

Other studies have also found snow albedo to decrease by 0.1 to 0.2 when subject to deposition of black carbon (Flanner et al., 2007; Hadley and Kirchstetter, 2012; Kokhanovsky et al., 2018), and a 20% decrease with simulated black carbon and dust (Zhang et al., 2017). In the current study, the snow plateau inter-annual albedo difference between 2018 (extreme wildfire season) and 2020 (no wildfires) was 0.050. The study of Mortimer and Sharp (2018) noted a decreasing trend of 0.0029 per year in the summer ice albedo of high arctic glaciers in relation to accelerated melt due to warming temperatures; however, in the current study, the difference in albedo between 2018 and 2020 was 0.148 for southeast-facing glaciers.

There are considerable differences in irradiance over the season at this fairly high latitude icefield, depending on slope and aspect. To analyze these differences, the albedo was converted into K* in W/m^2 (Figs. 10 and 11). The results showed, as expected, that the increase in absorbed shortwave irradiance over the level snow plateau is inversely correlated with the change in albedo, and that K* and its response to decreased albedo is strongly dependent on the overall slope and aspect. Glaciers with slopes facing southeast (S1 and S2) had a higher K* (771 W/m^2) than northeast-facing glaciers (565 W/m^2) (Athabasca, Saskatchewan, Dome), and southwest-facing glaciers (Castleguard, Columbia, S3, S4) had intermediate K* (756 W/m^2). Peak K* occurred in 2017-08-11 for all glaciers and the snow plateau (446 W/m^2), except for northeast-facing glaciers that had their peak K* in 2017-08-06.

Small-scale studies, for example that of Kaspari et al. (2015) on Mount Olympus, Washington, USA, discovered shortwave radiative forcing at the snow surface from black carbon and dust varied from 199 to 264 W/m^2. In addition, Nagorski et al. (2019) found radiative forcing values due to black carbon and dust on the snow of the Juneau Icefield, Alaska, USA ranging from 70 to 130 W/m^2. Likewise, the results of this study showed that the snow plateau had the highest shortwave radiative forcing (106 W/m^2) between 2017-08-06 and 2020-08-05. For glacier ice on the southeastern Tibetan Plateau, shortwave forcing values between 1 and 141 W/m^2 per year were found by Zhang et al. (2017), and the highest inter-annual shortwave forcing of 203 W/m^2 to southeast-facing glaciers from this study was found between 2018-08-13 and 2020-08-05.

The difference between K* with and without slope and aspect correction is shown in Fig. 12, which shows how slope and aspect impact K* for mountain icefields. Not accounting for slope and aspect in these environments caused an underestimation of K* of up to 285 W/m^2 on steep southwest-facing glaciers and an overestimation of up to 234 W/m^2 for steep northeast-facing glaciers. The analysis shows that the response of K* to aspect is stronger than to slope. It also shows that the response of K* to slope and aspect is more influenced by the atmospheric state (transmissivity) than to soot deposition using the Allen et al. (2006) parameterization and at a date-to-date time interval, since the dates with the lowest albedo were not necessarily the same as the dates of the highest slope and aspect influence on K*. The R^2 of the difference between K* with and without slope and aspect correction and transmissivity is high for all icefield subdivisions (from 0.63 to 0.87). This happens because the incoming diffuse radiation dominates the irradiance fluxes during low transmittance and increases K* isotropically, i.e., K* increases even for northern aspects (for example, on 2017-08-06). Conversely, the R^2 of the difference between K* with and without slope and aspect correction and albedo varies from 0.10 to 0.62. Nonetheless, Fig. 12 clearly shows that the annual influence of slope and aspect on K* increases during years of soot presence (2017, 2018, and 2019), especially for south-facing glaciers. Ignoring the effects of slope and aspect would have caused a K* underestimation during years of soot presence, which in turn would represent less shortwave energy available
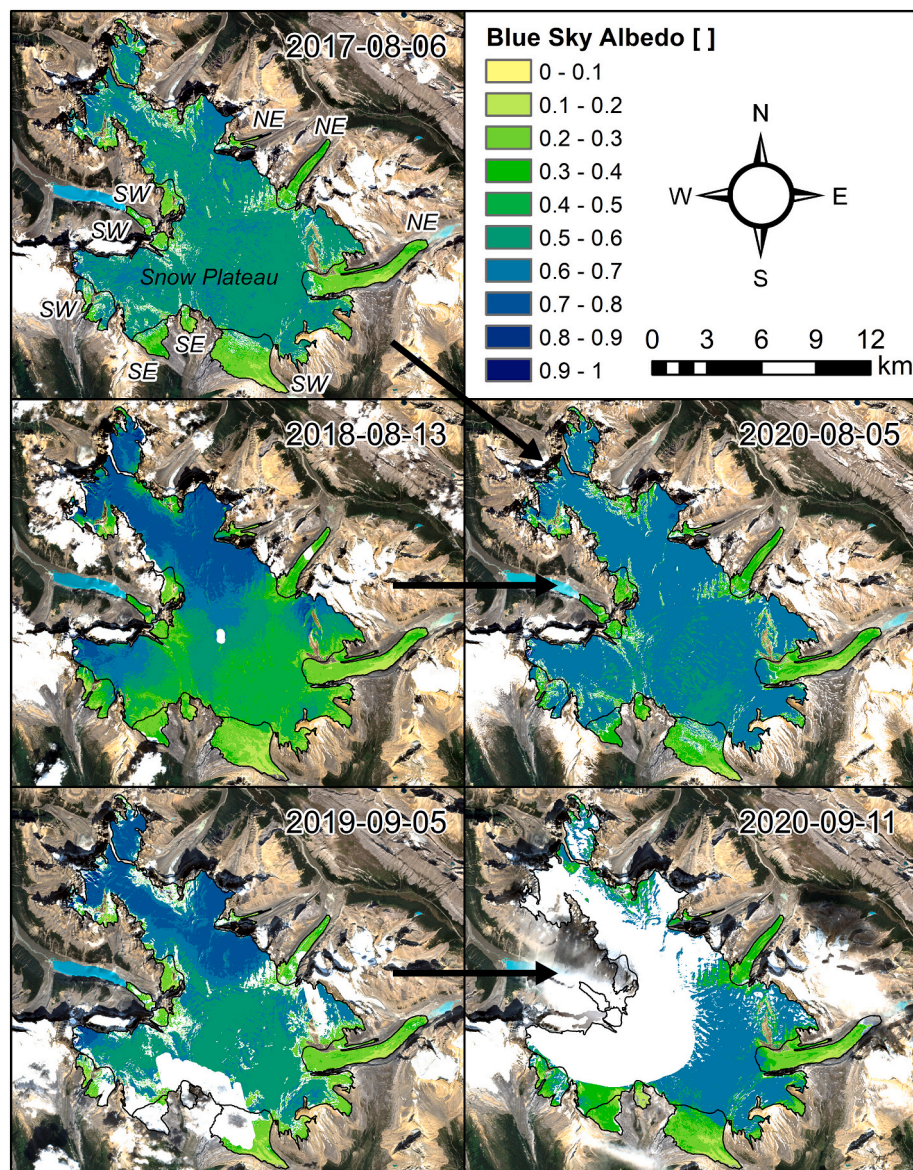
Fig. 8. Sentinel-2 blue-sky albedo retrievals for dates used for inter-annual comparisons. The black arrows indicate the pair of dates that were compared. Empty spaces inside the Columbia Icefield represent NA values. (For interpretation of the references to colour in this figure legend, the reader is referred to the web version of this article.)

to melt the snow and ice of the Columbia Icefield. This shows that small-scale errors in estimating soot impacts on melt energy due to not considering the topographic influence on irradiance, scale up to larger scales and are important for estimating icefield scale impacts of wildfire. Note that the 2018-08-21 date was not used to compute the above co-efficients of determination, since this date is clearly an outlier that was introducing overfitting into the analysis.

4. Conclusions

This study proposes a framework for the retrieval of snow and glacier ice albedo at the high spatial resolution required in high mountain environments and demonstrates the deployment of this framework in assessing the impact of wildfire soot deposition on snow and ice albedo decrease and K* in the Columbia Icefield, Canadian Rockies. The framework was proven to be suitable for retrieving high spatial resolution albedo for snow and ice at good accuracy levels ($R^2 = 0.68$), which suggests its use for applications that involve assessing the impact of wildfire on the mountain cryosphere. These findings show that the lowest spatially averaged albedo was 0.528 in 2017 for the snow plateau, and that most glaciers aspects had their minimum albedos in 2019 (NE: 0.261 and SW: 0.278). SE glaciers had their minimum albedo (0.258) in 2020, due to persistence of low albedo in 2020 and possibly due to under-sampling of this aspect during 2019. The largest inter-annual soot-induced decrease in albedo was 0.148 for southeast-facing glaciers and 0.050 for the snow plateau between 2018 and 2020. This widespread decrease in albedo generated a maximum spatially averaged K* of 446 W/m^2 for the snow plateau and 771 W/m^2 for southeast-facing glaciers in 2017. The largest inter-annual soot-induced shortwave radiative forcing was 203 W/m^2 for southeast-facing glaciers between 2018 and 2020, and 106 W/m^2 for the snow plateau between 2017 and 2020. This study also highlighted spatial differences in albedo response timing to wildfire soot deposition. It showed that glacier ice undergoes a more prolonged decrease in albedo even after fire activity has ceased, which is probably caused by the bio-albedo feedback, whereas snow albedo can be refreshed in the same year. The use of K* slope and aspect correction was also found to be essential for providing accurate representations of spatially-distributed K* in mountain icefields.
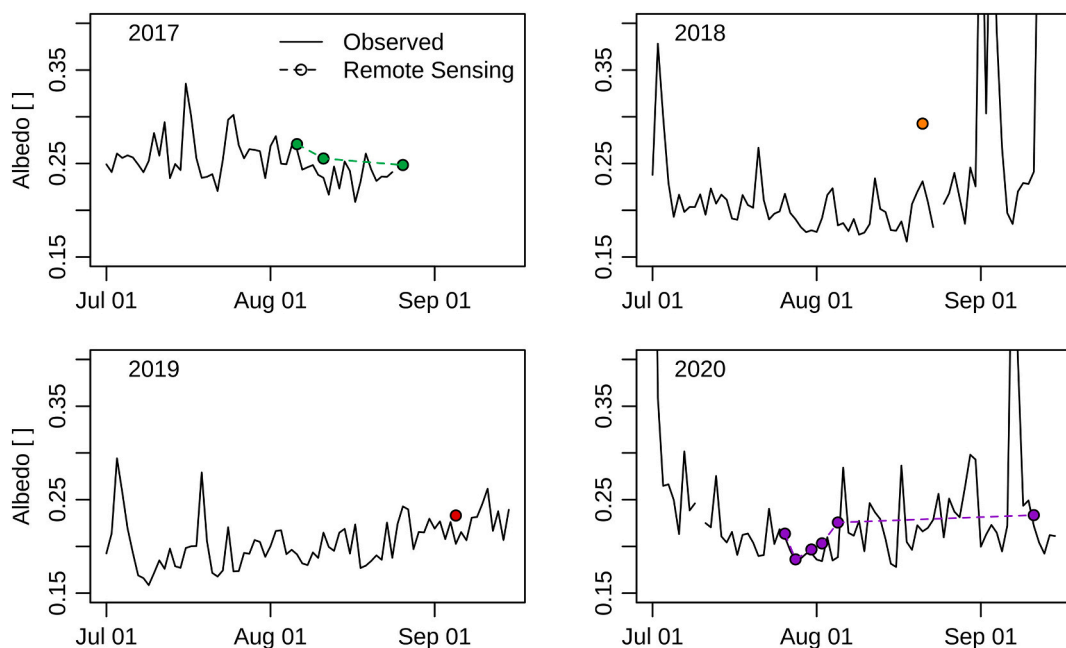
Fig. 9. Annual timeseries plots showing the observed albedo at 13:00:00 CST and the blue sky remote sensing albedo. (For interpretation of the references to colour in this figure legend, the reader is referred to the web version of this article.)
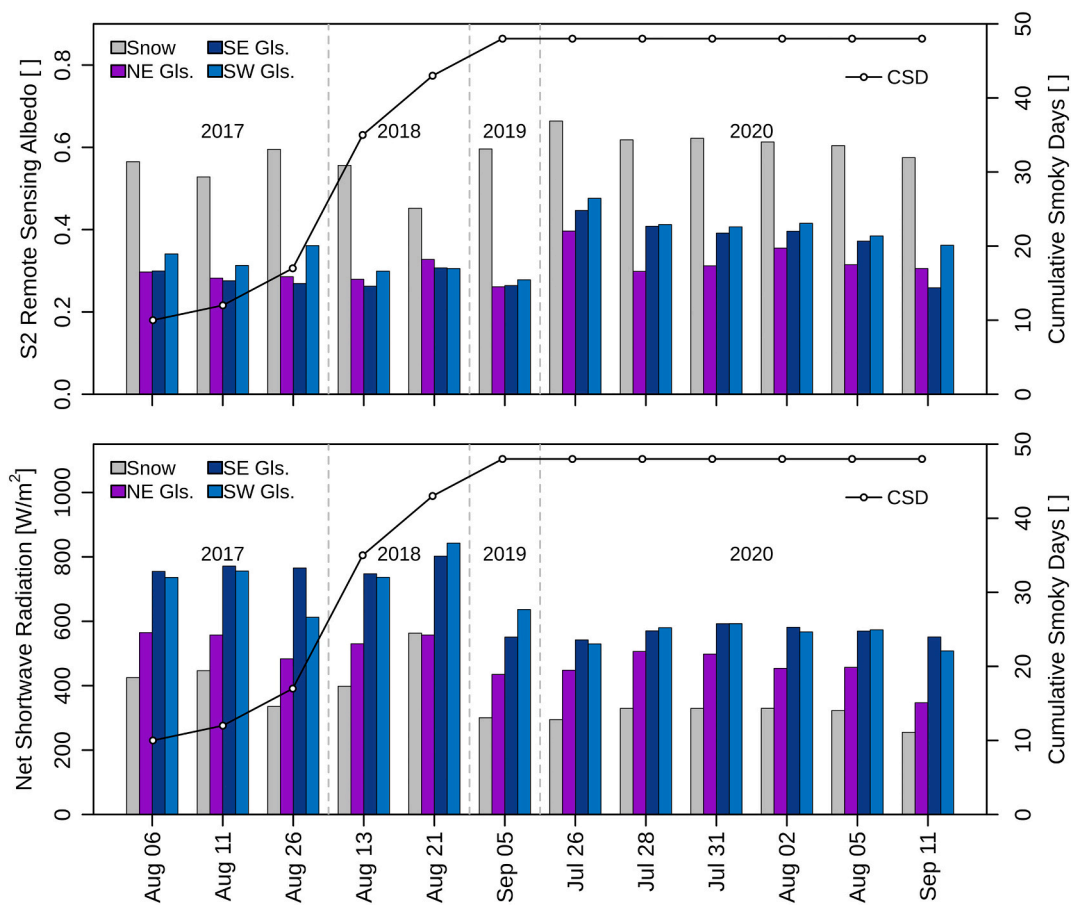

Fig. 10. Spatially averaged albedo and CSD (top panel), and K* and CSD (bottom panel).

Although this framework is sufficiently robust to be applied as presented herein, some limitations need to be considered. The quality of MODIS BRDF retrievals is extremely important for high spatial resolution albedo retrieval; therefore, it is suggested that the MODIS BRDF retrievals undergo a pre-evaluation process. More specifically, to ensure consistent high spatial resolution albedo retrieval, users are
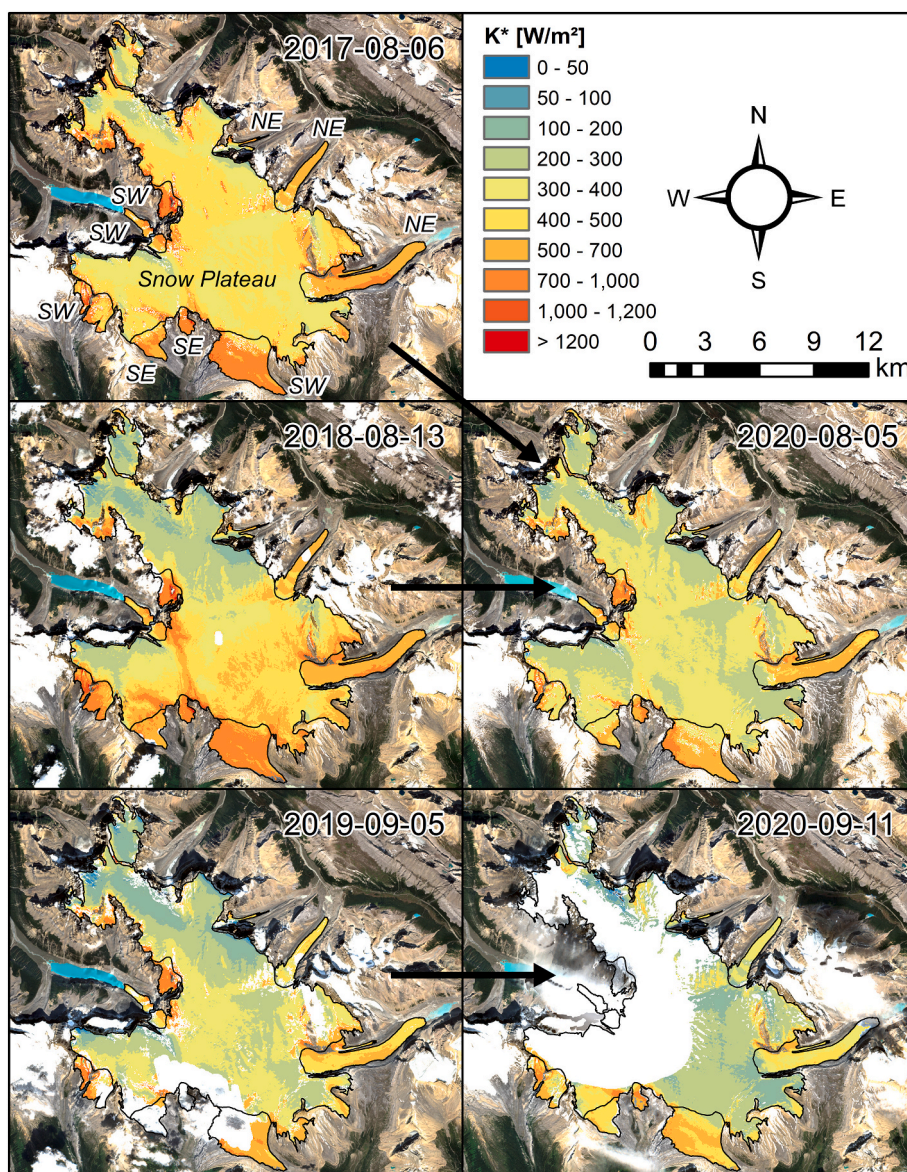
Fig. 11. Estimated K* corrected for slope and aspect effects for dates used for inter-annual comparisons. The black arrows indicate the pair of dates that were compared. Empty spaces inside the Columbia Icefield represent NA values.

encouraged to be cautious when using retrievals with a low number of clear MODIS observations within the 16-day BRDF retrieval window. This study showed that retrieving high quality BRDF pixels in regions with high cloud cover frequency is troublesome even using the RTLSR model, which was superior compared to the snow kernel model. A low number of high quality BRDF pixels can limit spatiotemporal analysis due to the scarce availability of high spatial resolution albedo estimates. Another important limitation to consider is the need to properly determine the number of cluster classes used in the classification process, and to assess whether this parameter may be more sensitive in other regional contexts. Moreover, whenever possible, an evaluation of whether the cloud-shadow screening processes adopted by MODIS and Sentinel-2 are able to properly separate snow from clouds and from cloud shadows is recommended to ensure the successful application of the framework.

This study shows that this framework has the potential to be applied in all kinds of applications that rely on a proper representation of spatiotemporal variations in snow and ice albedo. As more intense and widespread wildfire activity is predicted to occur as the climate warms, future research should focus on increasing the frequency of high spatial resolution albedo estimates retrieved in summer from potentially impacted cryospheric landscapes such as continental mountain snow and ice surfaces. Research focusing on improving cloud masks for MODIS and Sentinel-2 is expected to greatly decrease the uncertainties that clouds introduce in this type of albedo retrieval framework. Studies that use spatially-distributed hydrological models should assess whether the assimilation of albedo retrievals improves the overall accuracy of streamflow prediction and forecasting in cold regions. In addition, it is possible that the employed framework can be used with geospatial cloud computing tools, which would increase the number of applications. Finally, the large-area high spatial resolution observational albedo estimates developed in this study are expected to be extremely important for assessing the nonstationary impacts of climate change on water resources.

Description of author's responsibilities

André Bertoncini (AB) developed the framework used to retrieve high spatial resolution albedo from Sentinel-2 and assessed the impact of wildfire soot deposition on snow and ice albedo and K*. Caroline Aubry-Wake (CAW) helped process hydrometeorological data and performed
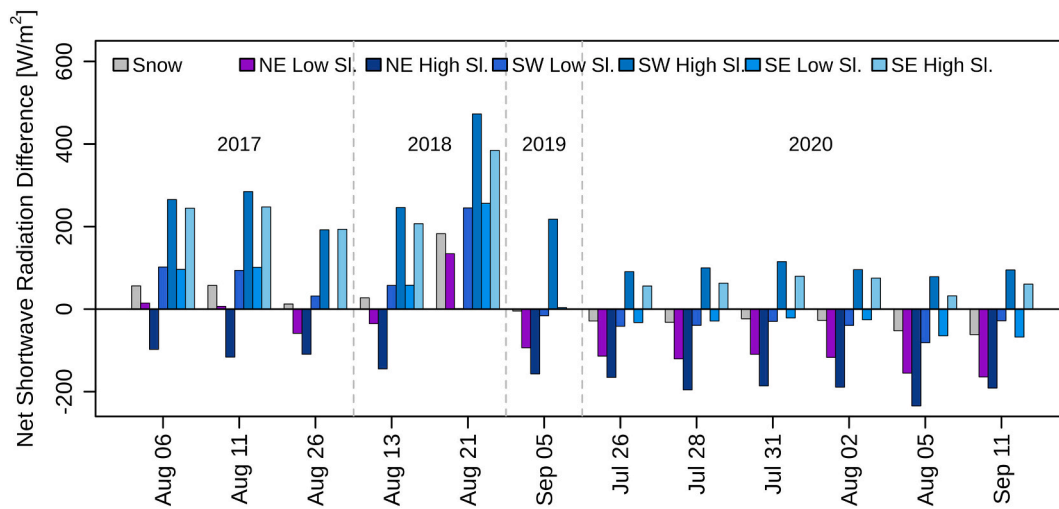
Fig. 12. Difference between K* with and without slope and aspect correction (with minus without correction). A positive difference means an underestimation of K* if not corrected for slope and aspect and vice-versa.

the CSD visual supervised classification from the timelapse camera. John W. Pomeroy (JWP) instrumented the glacier and CAW helped with station maintenance. All authors contributed to the hypotheses, manuscript conceptualization, writing, and editing.

Declaration of Competing Interest

The authors declare that they have no known competing financial interests or personal relationships that could have appeared to influence the work reported in this paper.

Acknowledgements

Appendix A. MODIS-Terra surface reflectance spectral response correction

Because MODIS-Terra instrument spectral response differs from those of Sentinel-2A and 2B, a spectral response correction was necessary to bring MODIS-Terra surface reflectance to the same level of Sentinel-2A and 2B surface reflectances. This correction was applied to MODIS-Terra surface reflectance before any BRDF calculation. The correction used the Spectral Band Adjustment Factors (SBAFs) for surface reflectance developed by Pearlman et al. (2003) and Scarino et al. (2016), which are available at: https://satcorps.larc.nasa.gov/cgi-bin/site/showdoc?mnemonic=HYPERION. This method calculates SBAF based on Hyperion spectra to determine the relationship between the surface reflectance of MODIS-Terra and Sentinel-2A and 2B for a particular band. The SBAFs used in this study are shown in Table A1 and had a minimum R^2 of 0.934. The SBAFs are landcover-dependent; therefore, they were retrieved for each landcover class corresponding to the MCD12Q1 MODIS landcover product. MCD12Q1 was used to determine which SBAF was applied for each MODIS-Terra surface reflectance pixel. MCD12Q1 is an annual product that represents our study area for the summer months; however, the landcover for 2020 is not available yet, and thus, the landcover for 2019 was used in 2020. This is a reasonable assumption since landcover does not change considerably at a yearly rate at a MODIS spatial resolution, as shown in Fig. A1.

Table A1
SBAF values for Sentinel-2A and 2B used in this study. The band names are for MODIS-Terra and the landcover classes follow the MCD12Q1 naming convention.

| Landcover class	Blue		Green		Red		NIR		SWIR1		SWIR2	
	SA	SB	SA	SB	SA	SB	SA	SB	SA	SB	SA	SB
Evergreen Needleleaf Forests	0.987	0.986	1.023	1.022	0.974	0.975	0.977	0.973	1.056	1.066	0.839	0.859
Deciduous Broadleaf Forests	0.987	0.987	1.021	1.020	0.979	0.980	0.970	0.966	1.058	1.068	0.857	0.875
Mixed Forests	0.983	0.983	1.023	1.022	0.970	0.970	0.977	0.973	1.058	1.069	0.811	0.836
Closed Shrublands	0.981	0.981	1.018	1.017	0.970	0.970	0.969	0.965	1.047	1.054	0.938	0.944
Open Shrublands	0.960	0.960	1.010	1.009	0.969	0.969	0.979	0.975	1.037	1.043	0.988	0.987
Woody Savannas	1.000	1.000	1.020	1.019	0.988	0.989	0.960	0.957	1.056	1.065	0.943	0.946
Savannas	0.982	0.982	1.012	1.011	0.983	0.984	0.961	0.958	1.050	1.058	0.972	0.972
Grasslands	0.955	0.956	1.012	1.012	0.970	0.970	0.978	0.974	1.045	1.052	0.935	0.943
Permanent Wetlands	0.959	0.959	1.018	1.017	0.973	0.973	0.983	0.978	1.055	1.065	0.812	0.834
Permanent Snow and Ice	0.947	0.948	1.018	1.017	0.973	0.973	0.995	0.988	1.063	1.076	0.672	0.714
Barren	0.922	0.924	0.982	0.984	0.955	0.955	0.973	0.969	1.029	1.032	1.068	1.052
Water Bodies	1.015	1.013	1.025	1.023	0.980	0.981	0.983	0.978	1.046	1.053	0.855	0.874
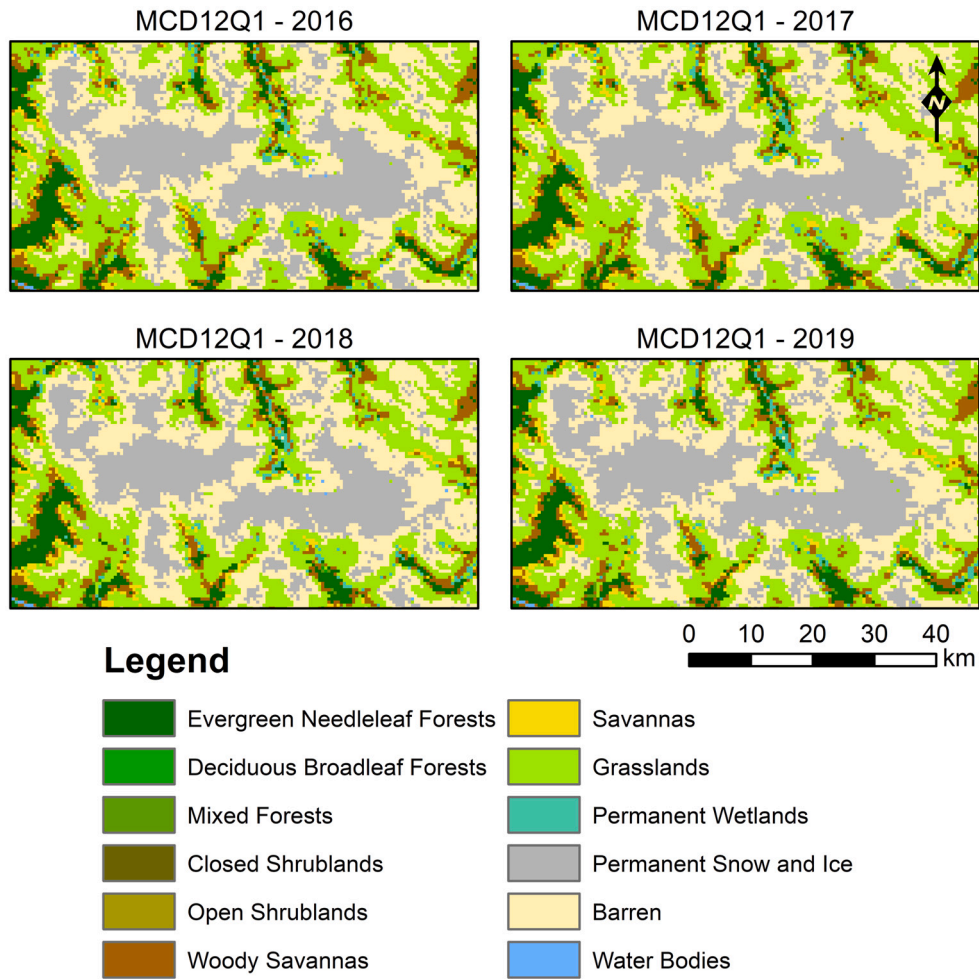
Fig. A1. Maps of yearly MCD12Q1 landcover, except for the 2020 year.

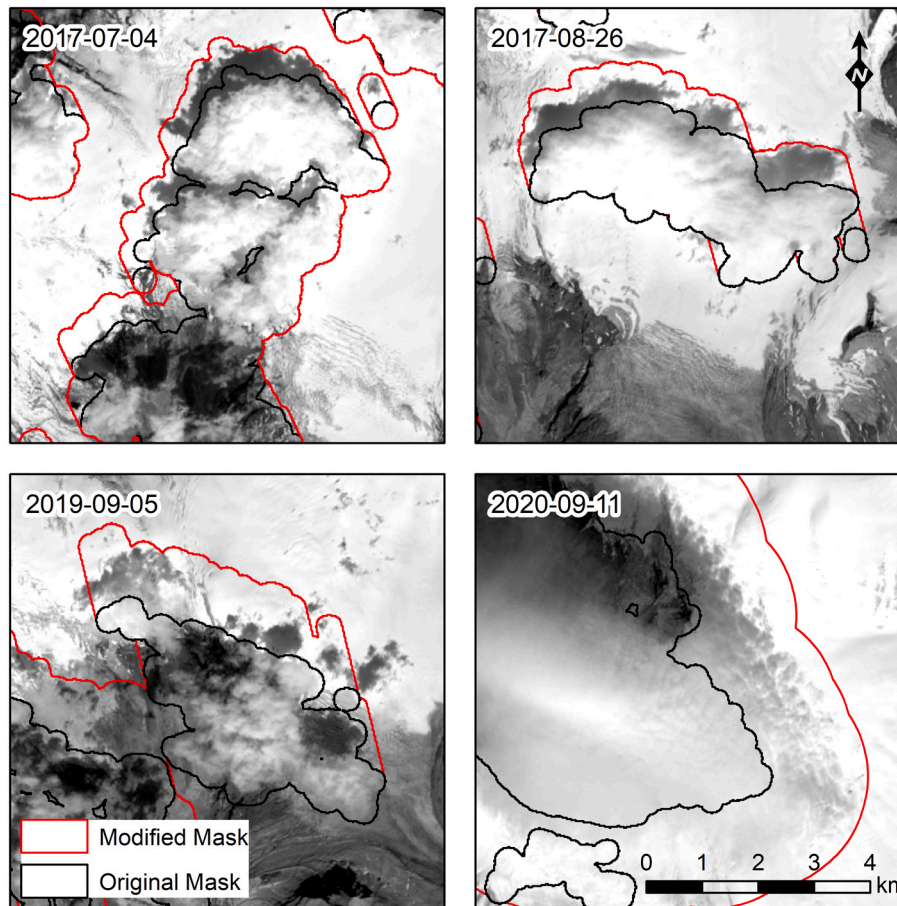## Appendix B. Correction of cloud-shadow screening algorithm

Fig. B1. Maps of the four cloud-shadow masks that required manual post-processing.

References

Allen, R.G., Trezza, R., Tasumi, M., 2006. Analytical integrated functions for daily solar radiation on slopes. Agric. For. Meteorol. 139, 55–73. https://doi.org/10.1016/j.agrformet.2006.05.012.

Allen, R.G., Tasumi, M., Morse, A., Trezza, R., Wright, J.L., Bastiaanssen, W., Kramber, W., Lorite, I., Robison, C.W., 2007. Satellite-based energy balance for mapping evapotranspiration with internalized calibration (METRIC)—applications. J. Irrig. Drain. Eng. 133, 395–406. https://doi.org/10.1061/(asce)0733-9437(2007)133:4(395).

Arnold, N.S., Rees, W.G., 2003. Self-similarity in glacier surface characteristics. J. Glaciol. 49, 547–554. https://doi.org/10.3189/172756503781830368.

Baars, H., Ansmann, A., Ohneiser, K., Haarig, M., Engelmann, R., Althausen, D., Hanssen, I., Gausa, M., Pietruczuk, A., Szkop, A., Stachlewska, I.S., Wang, D., Reichardt, J., Skupin, A., Mattis, I., Trickl, T., Vogelmann, H., Navas-Guzmán, F., Haefele, A., Acheson, K., Ruth, A.A., Tatarov, B., Müller, D., Hu, Q., Podvin, T., Goloub, P., Veselovskii, I., Pietras, C., Haeffelin, M., Fréville, P., Sicard, M., Comerón, A., García, A.J.F., Menéndez, F.M., Córdoba-Jabonero, C., Guerrero-Rascado, J.L., Alados-Arboledas, L., Bortoli, D., Costa, M.J., Dionisi, D., Liberti, G.L., Wang, X., Sannino, A., Papagiannopoulos, N., Boselli, A., Mona, L., D'Amico, G., Romano, S., Perrone, M.R., Belegante, L., Nicolae, D., Grigorov, I., Gialitaki, A., Amiridis, V., Soupiona, O., Papayannis, A., Mamouri, R.E., Nisantzi, A., Heese, B., Hofer, J., Schechner, Y.Y., Wandinger, U., Pappalardo, G., 2019. The unprecedented 2017-2018 stratospheric smoke event: decay phase and aerosol properties observed with the EARLINET. Atmos. Chem. Phys. 19, 15183–15198. https://doi.org/10.5194/acp-19-15183-2019.

Bastiaanssen, W.G.M., Menenti, M., Feddes, R.A., Holtslag, A.A.M., 1998. A remote sensing surface energy balance algorithm for land (SEBAL). 1. Formulation. J. Hydrol. 212–213, 198–212. https://doi.org/10.1016/S0022-1694(98)00253-4.

Bolch, T., Menounos, B., Wheate, R., 2010. Landsat-based inventory of glaciers in western Canada, 1985-2005. Remote Sens. Environ. 114, 127–137. https://doi.org/10.1016/j.rse.2009.08.015.

Chen, J., Anderson, K., Pavlovic, R., Moran, M.D., Englefield, P., Thompson, D.K., Munoz-Alpizar, R., Landry, H., 2019. The FireWork v2.0 air quality forecast system with biomass burning emissions from the Canadian Forest fire emissions prediction system v2.03. Geosci. Model Dev. 12, 3283–3310. https://doi.org/10.5194/gmd-12-3283-2019.

Combal, B., Isaka, H., 2002. The effect of small topographic variations on reflectance. IEEE Trans. Geosci. Remote Sens. 40, 663–670. https://doi.org/10.1109/TGRS.2002.1000325.

Cook, J.M., Tedstone, A.J., Williamson, C., McCutcheon, J., Hodson, A.J., Dayal, A., Skiles, M., Hofer, S., Bryant, R., McAree, O., McGonigle, A., Ryan, J., Anesio, A.M., Irvine-Fynn, T.D.L., Hubbard, A., Hanna, E., Flanner, M., Mayanna, S., Benning, L.G., Van As, D., Yallop, M., McQuaid, J.B., Gribbin, T., Tranter, M., 2020. Glacier algae accelerate melt rates on the South-Western Greenland ice sheet. Cryosphere 14, 309–330. https://doi.org/10.5194/tc-14-309-2020.

Cuffey, K.M., Paterson, W.S.B., 2010. The Physics of Glaciers, Fourth. ed. Butterworth-Heinemann/Elsevier, Burlington, MA, USA.

Da Ronco, P., De Michele, C., 2014. Cloud obstruction and snow cover in alpine areas from MODIS products. Hydrol. Earth Syst. Sci. 18, 4579–4600. https://doi.org/10.5194/hess-18-4579-2014.

de Magalhães, N., Evangelista, H., Condom, T., Rabatel, A., Ginot, P., 2019. Amazonian biomass burning enhances tropical Andean glaciers melting. Sci. Rep. 9, 1–12. https://doi.org/10.1038/s41598-019-53284-1.

Di Mauro, B., Garzonio, R., Baccolo, G., Franzetti, A., Pittino, F., Leoni, B., Remias, D., Colombo, R., Rossini, M., 2020. Glacier algae foster ice-albedo feedback in the European Alps. Sci. Rep. 10, 1–9. https://doi.org/10.1038/s41598-020-61762-0.

Doherty, S.J., Warren, S.G., Grenfell, T.C., Clarke, A.D., Brandt, R.E., 2010. Light-absorbing impurities in Arctic snow. Atmos. Chem. Phys. 10, 11647–11680. https://doi.org/10.5194/acp-10-11647-2010.

Duguay, C.R., 1995. An approach to the estimation of surface net radiation in mountain areas using remote sensing and digital terrain data. Theor. Appl. Climatol. 52, 55–68. https://doi.org/10.1007/BF00865507.

Ebrahimi, S., Marshall, S.J., 2016. Surface energy balance sensitivity to meteorological variability on Haig Glacier, Canadian Rocky Mountains. Cryosphere 10, 2799–2819. https://doi.org/10.5194/tc-10-2799-2016.

Ellis, C.R., Pomeroy, J.W., 2007. Estimating sub-canopy shortwave irradiance to melting snow on forested slopes. Hydrol. Process. 21, 2581–2593. https://doi.org/10.1002/hyp.6794.

Flanner, M.G., Zender, C.S., Randerson, J.T., Rasch, P.J., 2007. Present-day climate forcing and response from black carbon in snow. J. Geophys. Res. Atmos. 112, 1–17. https://doi.org/10.1029/2006JD008003.

Flanner, M.G., Zender, C.S., Hess, P.G., Mahowald, N.M., Painter, T.H., Ramanathan, V., Rasch, P.J., 2009. Springtime warming and reduced snow cover from carbonaceous particles. Atmos. Chem. Phys. 9, 2481–2497. https://doi.org/10.5194/acp-9-2481-2009.

Gardner, A.S., Sharp, M.J., 2010. A review of snow and ice albedo and the development of a new physically based broadband albedo parameterization. J. Geophys. Res. Earth Surf. 115, 1–15. https://doi.org/10.1029/2009JF001444.

Hadley, O.L., Kirchstetter, T.W., 2012. Black-carbon reduction of snow albedo. Nat. Clim. Chang. 2, 437–440. https://doi.org/10.1038/nclimate1433.

Hanes, C.C., Wang, X., Jain, P., Parisien, M.A., Little, J.M., Flannigan, M.D., 2019. Fire-regime changes in Canada over the last half century. Can. J. For. Res. 49, 256–269. https://doi.org/10.1139/cjfr-2018-0293.

Harder, P., Pomeroy, J., 2013. Estimating precipitation phase using a psychrometric energy balance method. Hydrol. Process. 27, 1901–1914. https://doi.org/10.1002/hyp.9799.

Heusser, C.J., 1956. Postglacial environments in the Canadian Rocky Mountains. Ecol. Monogr. 26, 263–302.

Hopkinson, C., Young, G.J., 1998. The effect of glacier wastage on the flow of the Bow River at Banff, Alberta, 1951-1993. Hydrol. Process. 12, 1745–1762.

Jiao, Z., Ding, A., Kokhanovsky, A., Schaaf, C., Bréon, F.M., Dong, Y., Wang, Z., Liu, Y., Zhang, X., Yin, S., Cui, L., Mei, L., Chang, Y., 2019. Development of a snow kernel to better model the anisotropic reflectance of pure snow in a kernel-driven BRDF model framework. Remote Sens. Environ. 221, 198–209. https://doi.org/10.1016/j.rse.2018.11.001.

Jiao, Z., Zhang, X., Bréon, F.M., Dong, Y., Schaaf, C.B., Román, M., Wang, Z., Cui, L., Yin, S., Ding, A., Wang, J., 2018. The influence of spatial resolution on the angular variation patterns of optical reflectance as retrieved from MODIS and POLDER measurements. Remote Sens. Environ. 215, 371–385. https://doi.org/10.1016/j.rse.2018.06.025.

Jolly, W.M., Cochrane, M.A., Freeborn, P.H., Holden, Z.A., Brown, T.J., Williamson, G.J., Bowman, D.M.J.S., 2015. Climate-induced variations in global wildfire danger from 1979 to 2013. Nat. Commun. 6, 1–11. https://doi.org/10.1038/ncomms8537.

Kaspari, S., Skiles, S.M.K., Delaney, I., Dixon, D., Painter, T.H., 2015. Accelerated glacier melt on snow dome, Mount Olympus, Washington, USA, due to deposition of black carbon and mineral dust from wildfire. J. Geophys. Res. 120, 2793–2807. https://doi.org/10.1002/2014JD022676.

Kim, Y., Hatsushika, H., Muskett, R.R., Yamazaki, K., 2005. Possible effect of boreal wildfire soot on Arctic Sea ice and Alaska glaciers. Atmos. Environ. 39, 3513–3520. https://doi.org/10.1016/j.atmosenv.2005.02.050.

Kirchmeier-Young, M.C., Gillett, N.P., Zwiers, F.W., Cannon, A.J., Anslow, F.S., 2019. Attribution of the influence of human-induced climate change on an extreme fire season. Earth's Futur. 7, 2–10. https://doi.org/10.1029/2018EF001050.

Klein, A.G., Hall, D.K., Riggs, G.A., 1998. Improving snow cover mapping in forests through the use of a canopy reflectance model. Hydrol. Process. 12, 1723–1744. https://doi.org/10.1002/(SICI)1099-1085(199808/09)12:10/11<1723::AID-HYP691>3.0.CO;2-2.

Kokhanovsky, A., Lamare, M., Di Mauro, B., Picard, G., Arnaud, L., Dumont, M., Tuzet, F., Brockmann, C., Box, J.E., 2018. On the reflectance spectroscopy of snow. Cryosphere 12, 2371–2382. https://doi.org/10.5194/tc-12-2371-2018.

Lee, W.L., Liou, K.N., 2012. Effect of absorbing aerosols on snow albedo reduction in the Sierra Nevada. Atmos. Environ. 55, 425–430. https://doi.org/10.1016/j.atmosenv.2012.03.024.

Lewis, P., 1995. Utility of kernel-driven BRDF models in global BRDF and albedo studies. Int. Geosci. Remote Sens. Symp. 2, 1186–1188. https://doi.org/10.1109/igarss.1995.521179.

Li, X., Strahler, A.H., 1992. Geometric-optical bidirectional reflectance modeling of the discrete crown vegetation canopy: effect of crown shape and mutual shadowing. IEEE Trans. Geosci. Remote Sens. 30, 276–292.

Li, X., Gao, F., Wang, J., Strahler, A., 2001. A priori knowledge accumulation and its application to linear BRDF model inversion. J. Geophys. Res. Atmos. 106, 11925–11935. https://doi.org/10.1029/2000JD900639.

Li, Z., Erb, A., Sun, Q., Liu, Y., Shuai, Y., Wang, Z., Boucher, P., Schaaf, C., 2018. Preliminary assessment of 20-m surface albedo retrievals from sentinel-2A surface reflectance and MODIS/VIIRS surface anisotropy measures. Remote Sens. Environ. 217, 352–365. https://doi.org/10.1016/j.rse.2018.08.025.

Lucht, W., Lewis, P., 2000. Theoretical noise sensitivity of BRDF and albedo retrieval from the EOS-MODIS and MISR sensors with respect to angular sampling. Int. J. Remote Sens. 21, 81–98. https://doi.org/10.1080/014311600211000.

Lucht, W., Schaaf, C.B., Strahler, A.H., 2000. An algorithm for the retrieval of albedo from space using semiempirical BRDF models. IEEE Trans. Geosci. Remote Sens. 38, 977–998. https://doi.org/10.1109/36.841980.

McKenzie Skiles, S., Flanner, M., Cook, J.M., Dumont, M., Painter, T.H., 2018. Radiative forcing by light-absorbing particles in snow. Nat. Clim. Chang. 8, 964–971. https://doi.org/10.1038/s41558-018-0296-5.

Mortimer, C., Sharp, M., 2018. Spatiotemporal variability of Canadian High Arctic glacier surface albedo from MODIS data, 2001-2016. Cryosphere 12, 701–720. https://doi.org/10.5194/tc-12-701-2018.

Mueller-Wilm, U., Devignot, O., Pessiot, L., 2019. S2 MPC Sen2Cor Configuration and User Manual. European Space Agency: Technical Report, Ref. S2-PDGS-MPC-L2A-SUM-V2.8.

Nagorski, S.A., Kaspari, S.D., Hood, E., Fellman, J.B., Skiles, S.M.K., 2019. Radiative forcing by dust and black carbon on the Juneau icefield, Alaska. J. Geophys. Res. Atmos. 124, 3943–3959. https://doi.org/10.1029/2018JD029411.

Painter, T.H., Bryant, A.C., McKenzie Skiles, S., 2012. Radiative forcing by light absorbing impurities in snow from MODIS surface reflectance data. Geophys. Res. Lett. 39, 1–7. https://doi.org/10.1029/2012GL052457.

Painter, T.H., Seidel, F.C., Bryant, A.C., McKenzie Skiles, S., Rittger, K., 2013. Imaging spectroscopy of albedo and radiative forcing by light-absorbing impurities in mountain snow. J. Geophys. Res. Atmos. 118, 9511–9523. https://doi.org/10.1002/jgrd.50520.

Pearlman, J.S., Barry, P.S., Segal, C.C., Shepanski, J., Beiso, D., Carman, S.L., 2003. Hyperion, a space-based imaging spectrometer. IEEE Trans. Geosci. Remote Sens. 41, 1160–1173. https://doi.org/10.1109/TGRS.2003.815018.

Román, M.O., Gatebe, C.K., Schaaf, C.B., Poudyal, R., Wang, Z., King, M.D., 2011. Variability in surface BRDF at different spatial scales (30m-500m) over a mixed agricultural landscape as retrieved from airborne and satellite spectral measurements. Remote Sens. Environ. 115, 2184–2203. https://doi.org/10.1016/j.rse.2011.04.012.

Roujean, J.-L., Leroy, M., Deschamps, P.-Y., 1992. A bidirectional reflectance model of the Earth's surface for the correction of remote sensing data. J. Geophys. Res. 97, 20455–20468. https://doi.org/10.1029/92JD01411.

Roy, D.P., Ju, J., Lewis, P., Schaaf, C., Gao, F., Hansen, M., Lindquist, E., 2008. Multi-temporal MODIS–Landsat data fusion for relative radiometric normalization, gap filling, and prediction of Landsat data. Remote Sens. Environ. 112, 3112–3130. https://doi.org/10.1016/j.rse.2008.03.009.

Scarino, B.R., Doelling, D.R., Minnis, P., Gopalan, A., Chee, T., Bhatt, R., Lukashin, C., Haney, C., 2016. A web-based tool for calculating spectral band difference adjustment factors derived from SCIAMACHY hyperspectral data. IEEE Trans. Geosci. Remote Sens. 54, 2529–2542. https://doi.org/10.1109/TGRS.2015.2502904.

Schaaf, C.B., Li, X., Strahler, A.H., 1994. Topographic effects on bidirectional and hemispherical reflectances calculated with a geometric-optical canopy model. IEEE Trans. Geosci. Remote Sens. 32, 1186–1193. https://doi.org/10.1109/36.338367.

Schaaf, C.B., Gao, F., Strahler, A.H., Lucht, W., Li, X., Tsang, T., Strugnell, N.C., Zhang, X., Jin, Y., Muller, J., Lewis, P., Barnsley, M., Hobson, P., Disney, M., Roberts, G., Dunderdale, M., Doll, C., Robert, P., Hu, B., Liang, S., Privette, J.L., Roy, D., 2002. First operational BRDF, albedo nadir reflectance products from MODIS. Remote Sens. Environ. 83, 135–148.

Schirmer, M., Pomeroy, J.W., 2020. Processes governing snow ablation in alpine terrain-detailed measurements from the Canadian Rockies. Hydrol. Earth Syst. Sci. 24, 143–157. https://doi.org/10.5194/hess-24-143-2020.

Seidl, R., Thom, D., Kautz, M., Martin-Benito, D., Peltoniemi, M., Vacchiano, G., Wild, J., Ascoli, D., Petr, M., Honkaniemi, J., Lexer, M.J., Trotsiuk, V., Mairota, P., Svoboda, M., Fabrika, M., Nagel, T.A., Reyer, C.P.O., 2017. Forest disturbances under climate change. Nat. Clim. Chang. 7, 395–402. https://doi.org/10.1038/nclimate3303.

Shuai, Y., Schaaf, C.B., Strahler, A.H., Liu, J., Jiao, Z., 2008. Quality assessment of BRDF/albedo retrievals in MODIS operational system. Geophys. Res. Lett. 35, 1–5. https://doi.org/10.1029/2007GL032568.

Shuai, Y., Masek, J.G., Gao, F., Schaaf, C.B., 2011. An algorithm for the retrieval of 30-m snow-free albedo from Landsat surface reflectance and MODIS BRDF. Remote Sens. Environ. 115, 2204–2216. https://doi.org/10.1016/j.rse.2011.04.019.

Smith, C.D., 2007. Correcting the wind bias in snowfall measurements made with a Geonor T-200B precipitation gauge and Alter wind shield. In: Proceedings of the 14th SMOI, San Antonio, 2007, p. 6.

Soenen, S.A., Peddle, D.R., Coburn, C.A., 2005. SCS+C: a modified sun-canopy-sensor topographic correction in forested terrain. IEEE Trans. Geosci. Remote Sens. 43, 2148–2159. https://doi.org/10.1109/TGRS.2005.852480.

Stamnes, K., Tsay, S.-C., Wiscombe, W., Jayaweera, K., 1988. Numerically stable algorithm for discrete-ordinate-method radiative transfer in multiple scattering and emitting layered media. Appl. Opt. 27, 2502. https://doi.org/10.1364/ao.27.002502.

Strugnell, N.C., Lucht, W., 2001. An algorithm to infer continental-scale albedo from AVHRR data, land cover class, and field observation of typical BRDFs. J. Clim. 14, 1360–1376. https://doi.org/10.1175/1520-0442(2001)014<1360:AATICS>2.0.CO;2.

Tennant, C., Menounos, B., 2013. Glacier change of the Columbia Icefield, Canadian Rocky Mountains, 1919-2009. J. Glaciol. 59, 671–686. https://doi.org/10.3189/2013JoG12J135.

Verstraete, M.M., Pinty, B., Myneni, R.B., 1996. Potential and limitations of information extraction on the terrestrial biosphere from satellite remote sensing. Remote Sens. Environ. 58, 201–214. https://doi.org/10.1016/S0034-4257(96)00069-7.

Viviroli, D., Kummu, M., Meybeck, M., Kallio, M., Wada, Y., 2020. Increasing dependence of lowland populations on mountain water resources. Nat. Sustain. 3, 917–928. https://doi.org/10.1038/s41893-020-0559-9.

Wang, Y., Li, X., Nashed, Z., Zhao, F., Yang, H., Guan, Y., Zhang, H., 2007. Regularized kernel-based BRDF model inversion method for ill-posed land surface parameter retrieval. Remote Sens. Environ. 111, 36–50. https://doi.org/10.1016/j.rse.2007.03.007.

Wang, D., Liang, S., He, T., 2014. Mapping high-resolution surface shortwave net radiation from landsat data. IEEE Geosci. Remote Sens. Lett. 11, 459–463. https://doi.org/10.1109/LGRS.2013.2266317.

Wang, Z., Erb, A.M., Schaaf, C.B., Sun, Q., Liu, Y., Yang, Y., Shuai, Y., Casey, K.A., Román, M.O., 2016. Early spring post-fire snow albedo dynamics in high latitude boreal forests using Landsat-8 OLI data. Remote Sens. Environ. 185, 71–83. https://doi.org/10.1016/j.rse.2016.02.059.

Wang, Z., Schaaf, C.B., Sun, Q., Shuai, Y., Román, M.O., 2018. Capturing rapid land surface dynamics with collection V006 MODIS BRDF/NBAR/albedo (MCD43) products. Remote Sens. Environ. 207, 50–64. https://doi.org/10.1016/j. rse.2018.02.001.

Wanner, W., Li, X., Strahler, A.H., 1995. On the derivation of kernels for kernel-driven models of bidirectional reflectance. J. Geophys. Res. 100, 21077–21089. https://doi. org/10.1029/95JD02371.

Williamson, S.N., Menounos, B., 2021. The influence of forest fires aerosol and air temperature on glacier albedo, western North America. Remote Sens. Environ. 267, 112732 https://doi.org/10.1016/j.rse.2021.112732.

Yasunari, T.J., Tan, Q., Lau, K.M., Bonasoni, P., Marinoni, A., Laj, P., Ménégoz, M., Takemura, T., Chin, M., 2013. Estimated range of black carbon dry deposition and the related snow albedo reduction over Himalayan glaciers during dry pre-monsoon periods. Atmos. Environ. 78, 259–267. https://doi.org/10.1016/j. atmosenv.2012.03.031.

Zhang, Y., Kang, S., Cong, Z., Schmale, J., Sprenger, M., Li, C., Yang, W., Gao, T., Sillanpää, M., Li, X., Liu, Y., Chen, P., Zhang, X., 2017. Light-absorbing impurities enhance glacier albedo reduction in the southeastern Tibetan plateau. J. Geophys. Res. 122, 6915–6933. https://doi.org/10.1002/2016JD026397.